

## Polarization angle tailored multitasking metasturcure: electromagnetically induced transparency, electromagnetically induced absorption, linear-to-circular polarization conversion

You Lv, Fang-Yao Fang, Yu-Jing Yin & Hai-Feng Zhang

To cite this article: You Lv, Fang-Yao Fang, Yu-Jing Yin & Hai-Feng Zhang (2023): Polarization angle tailored multitasking metasturcure: electromagnetically induced transparency, electromagnetically induced absorption, linear-to-circular polarization conversion, Waves in Random and Complex Media, DOI: [10.1080/17455030.2023.2222854](https://doi.org/10.1080/17455030.2023.2222854)

To link to this article: <https://doi.org/10.1080/17455030.2023.2222854>



Published online: 09 Jun 2023.



[Submit your article to this journal](#)



Article views: 4



[View related articles](#)



[View Crossmark data](#)



# Polarization angle tailored multitasking metasturcure: electromagnetically induced transparency, electromagnetically induced absorption, linear-to-circular polarization conversion

You Lv<sup>a</sup>, Fang-Yao Fang<sup>b</sup>, Yu-Jing Yin<sup>c</sup> and Hai-Feng Zhang<sup>a</sup>

<sup>a</sup>College of Electronic and Optical Engineering & College of Flexible Electronics (Future Technology), Nanjing University of Posts and Telecommunications, Nanjing, People's Republic of China; <sup>b</sup>Portland Institute, Nanjing University of Posts and Telecommunications, Nanjing, People's Republic of China; <sup>c</sup>College of Telecommunications & Information Engineering, Nanjing University of Posts and Telecommunications, Nanjing, People's Republic of China

## ABSTRACT

In this work, simultaneous implementation of electromagnetically induced transparency (EIT), electromagnetic induced absorption (EIA), and linear-to-circular polarization conversion (LTCPC) in the terahertz band is proposed in a metasturcure (MS) associated with tailoring the polarization angle ( $\theta$ ). The linear polarization (LP) waves with different  $\theta$  can trigger different phenomena. EIT can be achieved with the incidence of transverse electric (TE) waves ( $\theta = 0^\circ$ ), transverse magnetic (TM) waves ( $\theta = 90^\circ$ ) cause the appearance of EIA, while a LP wave with  $\theta = 45^\circ$  induces the appearance of the LTCPC phenomenon. For TE waves, the EIT transparent window accompanied by the slow light effect has emerged from 0.288 to 0.797 THz, where the maximum group delay has arrived at 2.51 ps. For TM waves, an absorption peak of EIA is observed at 0.497 THz. The LTCPC phenomenon is well obtained with  $\theta = 45^\circ$  at 0.399 and 0.634 THz, where the transmission coefficient highly reaches 0.571 and 0.650. The optimal axis ratios (ARs) of LTCPC are 2.08 dB at 0.389 THz and 2.18 dB at 0.634 THz, respectively. Noteworthy, the two-oscillator and circuit models are adopted for the theoretical analysis of the EIT and EIA, and the conclusions obtained are in general agreement with the simulation results.

## ARTICLE HISTORY


Received 17 February 2023  
Accepted 29 May 2023

## KEYWORDS

Metastrutures;  
polarization-tailored device;  
electromagnetically induced transparency;  
electromagnetic induced absorption; linear-to-circular polarization conversion

## 1. Introduction

Metastructure (MS), which can be acted as multifunctional metamaterials, has attracted a lot of attention due to its ability to generate electromagnetic responses that are unattainable in nature [1]. Electromagnetically induced transparency (EIT), arising from the destructive interference between different atomic leap channels, is an inherent quantum interference in three-atom systems [2]. In recent years, EIT has been extensively researched, enabling opaque media to be narrowly transparent and accompanied by intense dispersion and

**CONTACT** Hai-Feng Zhang  hanlor@163.com, hanlor@njupt.edu.cn

strong slow light effects [3,4]. EIT in most quantum systems requires incredibly demanding experimental circumstances, including extremely low temperatures and super-bumps of laser light, which basically cannot be implemented and applied to physical devices. However, in 2008, Zhang et al. successfully introduced the EIT effect to electromagnetic MSs [5]. Since then, due to its unique properties, EIT has been greatly exploited in slow-light devices [3,4], optical switches [6,7], photon storage, and nonlinear self-enhancement [8–10]. EIT is mainly generated by [11–13] bright-dark mode coupling alternately, bright-bright mode coupling [14,15]. The former is mainly formed by destructive interference, while the formation is due to the influence of weak hybridization on bright modes.

Electromagnetically induced absorption (EIA), which arises from atomic interference in quantum systems and is a complimentary effect to EIT, resulting in a sharp absorption window in a section of the transparent spectrum [16]. Unlike EIT, EIA is due to constructive interference rather than destructive interference. EIA was first experimentally studied in MSs by Sun et al. [17]. Tassin et al. [18] introduced a radiative two oscillator model to explain the absorption and scattering characteristics, and systematically showed that the transition from EIT to EIA (and vice versa) is accomplished by reducing the dissipative damping of the radiative state and increasing the dissipative damping of the dark mode [19]. And constructive interference is achieved by weakening the coupling. In addition, phase-shift modulation is a wonderful pathway for EIA in MSs, and A triple-coupling method for asymmetric MS was also discovered by Xu et al. [20], allowing for coherence augmentation. This mechanism is comparable to the temporal coupling principle outlined for ring bus architectures and triple resonators, and this narrow absorption EIA peak can also be explored in optical fields. Although both EIT and EIA are atomic level interference, and there have been previous works to integrate EIT and EIA into one device, most of these works were done with vanadium dioxide, graphene, or photosensitive materials in MSs [21,22], which is quite difficult to realize in practice. It is worth mentioning that the present work has a strong polarization-selective feature, showing two completely opposite properties for two different linearly polarized (LP) waves. for the transverse electric (TE) wave, which is defined as the LP waves with polarization angle (PA) ( $\theta = 0^\circ$ ), the MS associated with  $\theta = 0^\circ$  exhibits EIT characteristics, while EIA behaviors can be observed easily with the incidence of transverse magnetic (TM) waves ( $\theta = 90^\circ$ ).

Furthermore, since the unique electromagnetic properties of MSs, many polarization converters have also been reported [23–26], where the remarkable adaptability of the circular polarization (CP) wave in signal transmission and reception, the linear-to-circular polarization conversion (LTCPC) behaviors [27,28] have been studied in depth. Although polarization conversion achieved using MSs can well solve the thickness problem caused by the electrically thin size of MSs, most polarization systems of MSs still suffer from large transmission losses [29]. Sun et al. [30] exploited unusual optical transmission and tunneling effects to control the polarization state of electromagnetic waves using anisotropic transparent MSs. However, the proposed structure consisting of a three-layer MS is quite complex and hinders the integration with photonic systems. Recently, a plasmonic MS is designed to achieve polarization conversion [23], which can effectively reduce the loss of polarization conversion and enhance the performance. Nevertheless, it is rarely possible to change the electromagnetic wave polarization state in a balanced way in EIT and EIA MSs. Additionally, there are relatively few studies based on the ability of EIT and EIA to obtain LTCPC better. Herein, the conversion of three different phenomena (EIT, EIA, and LTCPC)

can be achieved by changing the PA of the incident LP waves, achieving a breakthrough in the PA control of multitasking devices.

In this paper, a MS based on EIT and EIA is proposed and also enables a LTCPC phenomenon with different  $\theta$ , where EIT ( $\theta = 0^\circ$ ), EIA ( $\theta = 90^\circ$ ), and LTCPC ( $\theta = 45^\circ$ ) can be controlled by incident LP waves. Compared with the conventional transmissive LTCPC, the destructive interference of EIT creates a highly transparent window that can considerably increase transmission efficiency and provide an operable platform for the integration of other functions. Moreover, considering the possible energy loss of overmastering electromagnetic wave polarization, polarization tunability is crucial in practical applications, particularly for modulators or selectors. Additionally, channel multiplexing, radome, and other frequency modulation settings are more commonplace with dual-band polarization. Additionally, channel multiplexing, radome, and other frequency modulation settings are more commonplace with dual-band polarization. Therefore, a dual-band polarization phenomenon incorporating efficient EIT and EIA effects has promising applications in MS. In this work, it is demonstrated that this implementation of polarization conversion phenomenon with frequencies and transmission coefficients located at 0.389 THz and 0.571, 0.634 THz, and 0.650, respectively. In the terahertz (THz) region, the EIT transparent window accompanied by the slow light effect has emerged from 0.288 THz to 0.797 THz with a relative bandwidth of 18.5% with significant group delay (GD) close to 144 ps and high transmission coefficients for TE waves, and the sharp absorption peak of EIA at 0.497 THz has reached 90.5% for TM waves.

## 2. Structure design and simulation

### 2.1. Structure design

It is schematically explained how the MS array periodogram and the final integrated configuration work in Figure 1(a), and the operating mode of the MS can also be observed in Figure 1(a). The proposed MS consists of a gold (conductivity  $\sigma = 4.561 \times 10^7$  S/m) [31] double-split ring (DSR), a four-split ring (FSR), and a barbell-shaped patch (BSP), which are all etched on both sides of the silicon (relative dielectric constant  $\epsilon_r = 11.7$ ) [32] substrate as displayed in Figure 1(b). Gold patches can be fixed to the surface of the dielectric substrate by E-beam evaporation deposition [33,34]. Figure 1(c) illustrates the relationship between the incident angle ( $\beta$ ) and PA ( $\theta$ ) and the coordinate axes. The incident waves presented in this paper are all incident vertically ( $\beta = 0^\circ$ ), unless specifically discussed. For TE waves, the electric and magnetic fields are oriented in the  $x$ - and  $y$ -axis directions, respectively, while for TM waves, in contrast to TE waves, the electric and magnetic fields are oriented in the  $y$ - and  $x$ -axis directions. The edge length of the cell structure of MS is  $p = 150 \mu\text{m}$ . The specific structural parameters will be shown in Table 1. The proposed MS is simulated in CST STUDIO SUITE and the unit cell boundary constraint has been adopted for the  $x$ -axis and  $y$ -axis, while the  $z$ -axis is open (add space) (Figure 2).

### 2.2. The analysis of EIT phenomenon

Figure 3 provides preliminary individual stimulation and surface current distribution of DSR and FSR irradiated by TE waves. The transmission response (see Figure 3(a,c)) and the

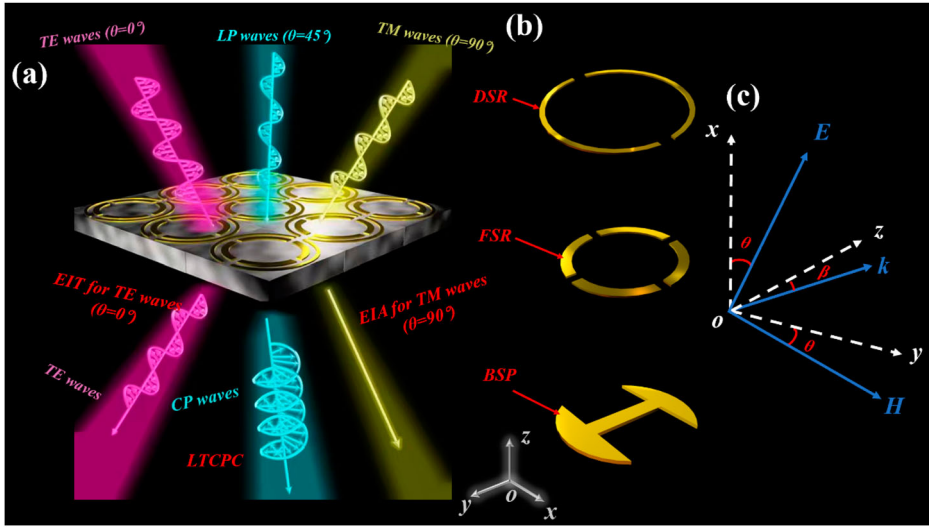


**Figure 1.** (a) Array periodogram and final integration configuration for MS, (b) diagrams of DSR, FSR and BSP, (c) the plot of PA and incident angle versus coordinates.

**Table 1.** Detailed geometric parameters for the MS.

Parameters	Value ( $\mu\text{m}$ )	Parameters	Value ( $\mu\text{m}$ )
$h$	10	$g$	10
$h_1$	0.2	$g_1$	15
$h_2$	0.2	$w$	10
$r$	68	$w_1$	5
$r_1$	49	$a$	50
$r_2$	40	$b$	10

surface currents (see Figure 3(b,d)) jointly specified that DSR and FSR can be directly excited by incident TE waves, demonstrating that both DSR and FSR are bright modes. For DSR, a significant response can be captured at 0.292 THz and the corresponding transmission amplitude is 0.012 with a smaller Q value of 1.16 (the quality factor of the fundamental resonance modes  $Q = f/\Delta f$ , where  $f$  is the resonance frequency,  $\Delta f$  means the half-maximum bandwidth) [35] as exhibited in Figure 3(a). In Figure 3(b), most of the energy is distributed on both sides of the DSR, inducing the formation of two electric dipoles, and the current is flowing in the positive direction of the y-axis. It is clearly revealed in Figure 3(c) that FSR produces a strong resonance at 0.841 THz with a transmission amplitude of 0.024 with a larger Q value of 3.73. Besides, the dispersion of the relevant surface currents amply demonstrated the energy is focused on four-quarter circles of FSR, and the current flows are in the negative direction of the y-axis. However, it is obvious from Figure 4(a) that the BSP is basically unable to couple the incident TE waves in the range from 0.2 THz to 0.9 THz. It is clearly obtained from Figure 4(b,c) that both bright modes (DSR and FSR) cannot couple the BSP under TE wave, so the BSP is not considered a dark mode either.

To facilitate the understanding of EIT, the formation process of EIT is shown in Figure 5. The resonance results of DSR and FSR with BSP are given in stages 1 and 2, and the final results of EIT where DSR, FSR and BSP have been concentrated in one unit cell are given in

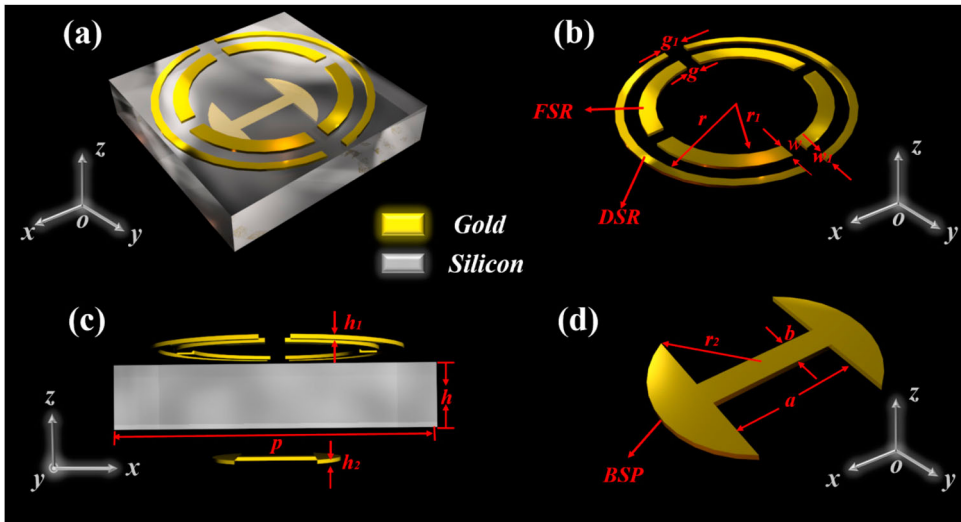


**Figure 2.** (a) The unit cell of the MS, (b) schematic diagrams of DSR and FSR, (c) the front view of MS, and (d) the stereoscopic view of the BSP.

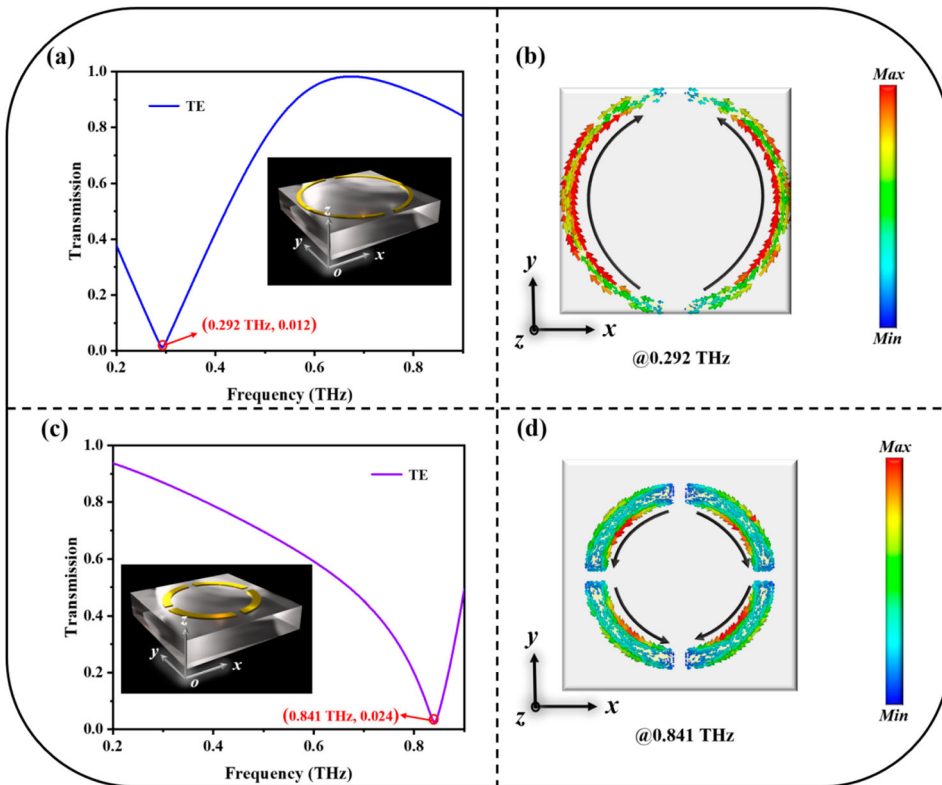


**Figure 3.** With the incidence of TE waves, the transmission response of DSR in (a) and FSR in (c), and the corresponding surface currents of DSR in (b) and FSR in (d).

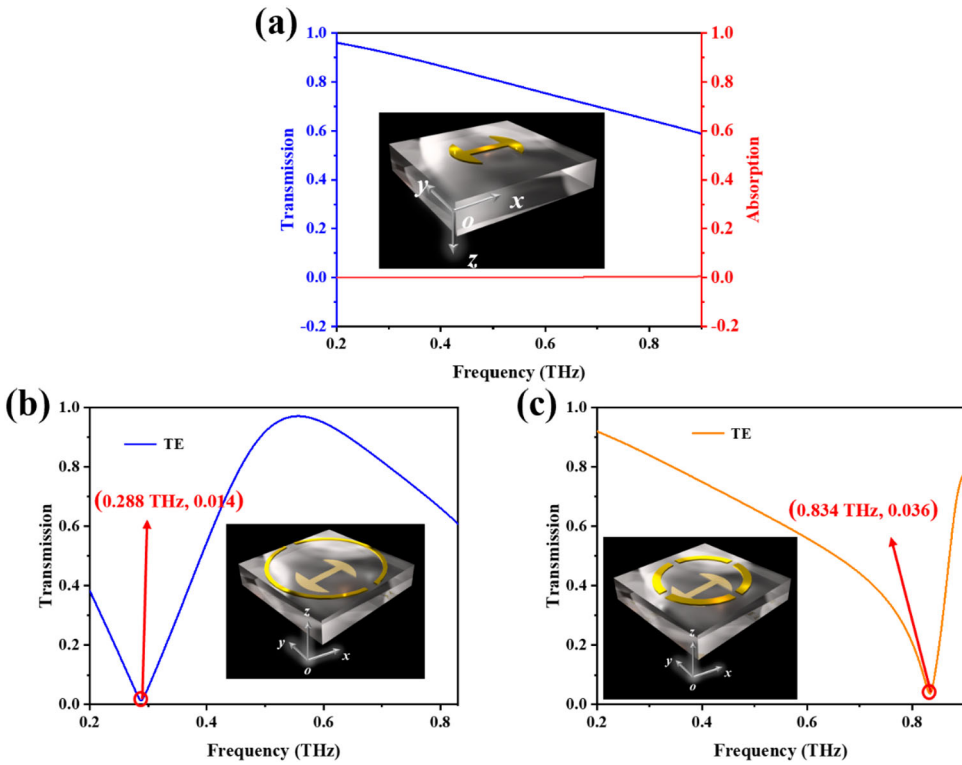


**Figure 4.** (a) The transmission and absorption curve of BSP between 0.2 and 0.9 THz for the TE waves, (b) the transmission response of DSR and BSP together under TE wave incidence, and (c) the transmission response of FSR and BSP.

stage 3. The resonant frequencies of DSR and FSR are similar and there is a certain difference in Q values, indicating that the EIT phenomenon can be formed theoretically. Hence, with the incidence of TE waves, the EIT phenomenon emerges naturally. As is displayed in Figure 6(a), a high transparency window (transmission amplitude above 0.9) between 0.441 THz and 0.531 THz is produced with a relative bandwidth of 18.5% arising from the destructive interference of DSR and FSR.

To better illustrate the potential principle of the EIT behavior, the surface current and electric field distributions at 0.288 THz, 0.480 THz, and 0.797 THz are analyzed and elaborated on (see Figure 6). It is easily observed from Figure 6(b) that the distribution of the MS surface currents at 0.288 THz is attributed to the fact that the DSR can be directly coupled to the incident field, triggering the generation of electric dipoles, while the current effects of FSR and BSP are much weaker. Similarly, at 0.797 THz, the majority of the energy is localized to the FSR in Figure 6(c), while the DSR and BSP barely interact with the incident field just as exhibited in Figure 6(d). However, the current flow on the DSR and FSR is completely opposite at 0.480 THz and the current on the FSR is significantly weaker compared to that at 0.797 THz, which means the energy on the FSR largely suppressed by the DSR, thus generating destructive interference similar to the triple atomic level. It is worth noting that the surface currents of the BSP at these three frequency points are extremely weak, proving that the

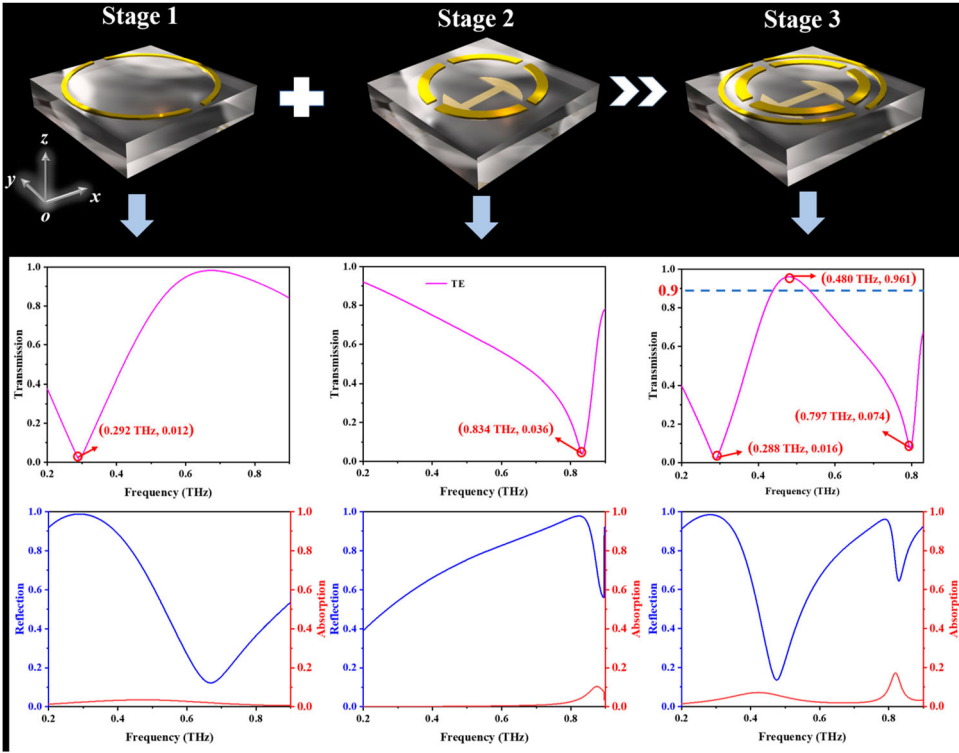


**Figure 5.** The forming process of EIT behavior for the TE waves.

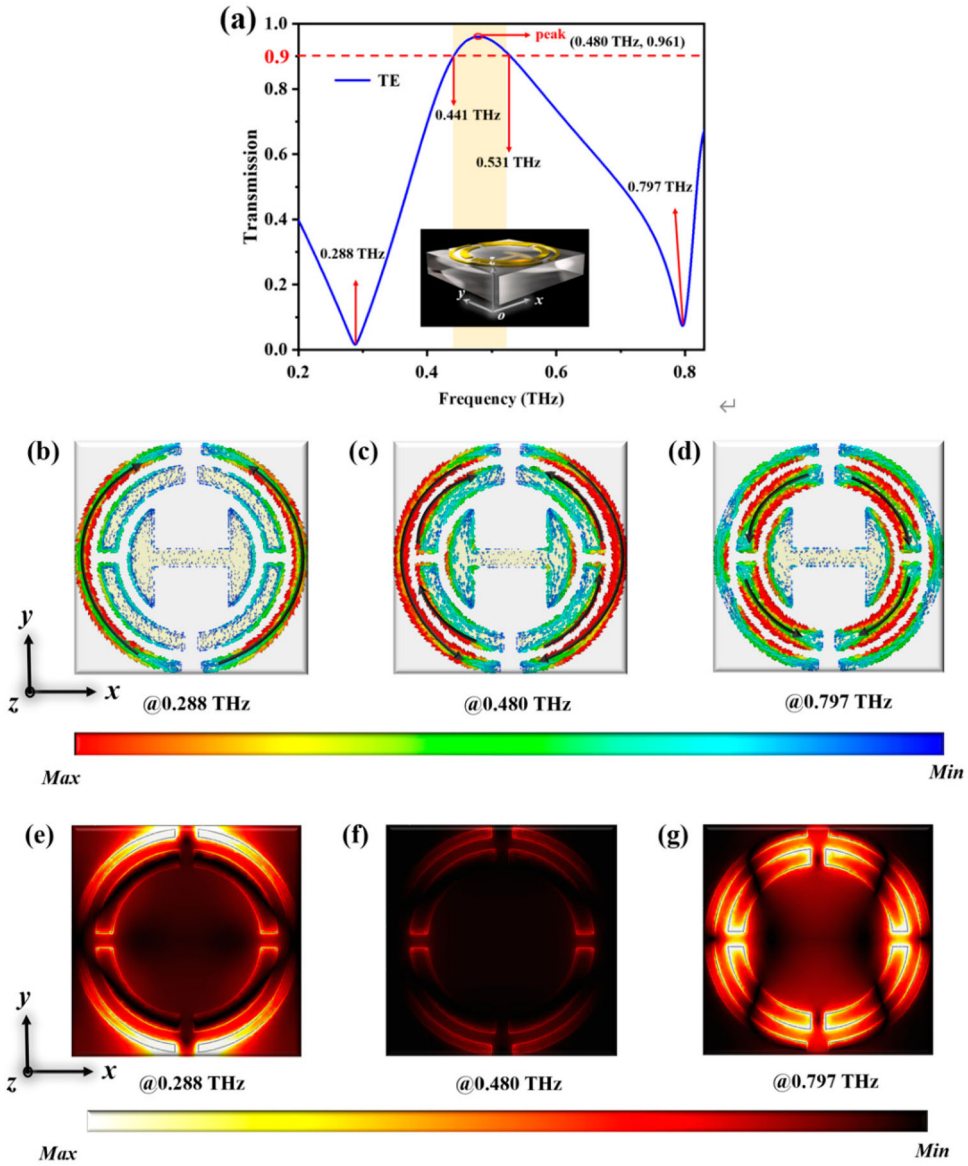
BSP is unable to produce a resonant response in this frequency band for TE waves. Therefore, a broad and high transparency window over 0.9 is produced, spanning from 0.441 THz to 0.531 THz with a relative bandwidth of 18.5% as exhibited in Figure 6(a).

Figure 6 also displays the electric field distribution at different frequencies, and it is evident that the accumulation of the electric field is essentially along the  $y$ -axis direction of the DSR resulting from self-coupling with the incident electric field, which leads to a transmission dip at 0.288 THz (see Figure 6(e)). As opposed to that, it is not difficult to see that another transmission dip at 0.797 THz is caused by the electric field aggregation on the FSR (exhibited in Figure 6(g)). For the transmission peak at 0.480 THz at the transparency peak in Figure 6(f), the near-field coupling significantly suppresses the induced electric fields on the DSR and FSR, which suggests the generation of destructive interference akin to the classical three-energy atomic system and is essential for the formation of the broadband EIT, supporting the principle of EIT formation once more.

Besides, the EIT phenomenon is accompanied by a more pronounced slow light effect, which refers to the phenomenon wherein dispersion causes the group speed of light to be lower than the speed of light in a vacuum. GD and group index (GI) are calculated from the phase transition at the corresponding transmission dips as shown in Figure 7(a), which is considered to be the key to measuring the EIT characteristics. The corresponding calculations of GD and GI are presented in Equations (1) and (2) [36,37].

$$t_{GD} = -\frac{\partial \varphi}{\partial \omega} \quad (1)$$





**Figure 6.** (a) The transmission response of EIT behavior for the TE waves, the surface current response of the EIT behavior (b) at 0.288 THz, (c) at 0.480 THz and (d) at 0.797 THz, and the electric field distribution results ( $z = 10.4\mu\text{m}$ ) of the EIT behavior (e) at 0.288 THz, (f) at 0.480 THz and (g) at 0.797 THz.

$$n_{GI} = \frac{c}{h} t_{GD} \quad (2)$$

Here,  $\varphi$  and  $\omega$  are defined as the transmission phase and angular frequency, respectively.  $c$  and  $h$  mean the light speed and the thickness of the MS.  $t_{GD}$  and  $n_{GI}$  stand for the concrete values of GD and GI. According to the calculation results in Figure 7(b,c), the maximum GD and GI are 2.51 ps and 72.5, respectively, which can be applied in optical communication [38] and tunable slow light devices [13].

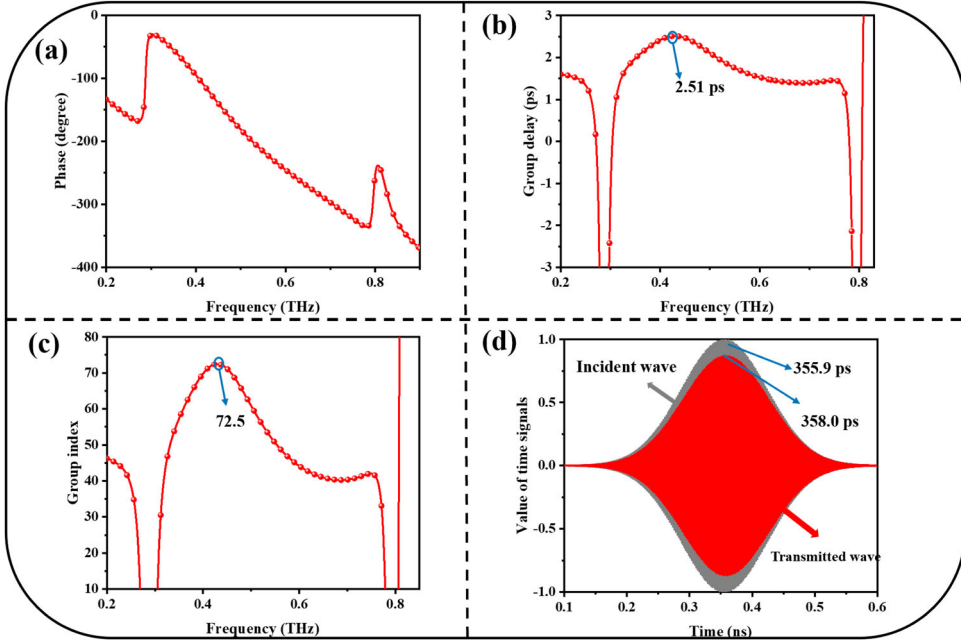


**Figure 7.** For TE waves, (a) the transmission phase of MS (b) the curve of GD, (c) the GI of EIT, and (d) simulation of a typically propagated Gaussian pulse's time development around a given MS at 0.430 THz with maximum GD.

To better verify the validity of the group time delay, a Gaussian-shaped pulse centered at 0.430 THz can be simulated on the basis of the finite difference time domain method (FDTD) simulation, as shown in Figure 7(d). The transmitted pulse's peak occurs at 358.0 ps, which is close to 0.430 THz, whereas the incident pulse's peak appears at 355.9 ps. as a result, the transmitted pulse is delayed by 2.1 ps. In addition, the GD in Figure 7(b) is about 2.51 ps near 0.430 THz and the corresponding Gi is 72.5. since the group time delay in Figure 7(b), the GD is built on a frequency domain algorithm, and the time domain algorithm is the basis of the GD in Figure 7(b), that is why an algorithmic difference occurs in the calculation. The slow light effect of the EIT phenomena is still reflected in the GD despite the differences. More significantly, the dispersion features of the EIT behavior result in the transmitted pulse through the EIT MS becoming wider than the incident pulse. Overall, the results demonstrate that the proposed EIT MS supports slow light propagation. In addition, the proposed EIT structure has many potential applications in the field of slow light.

In addition, to further understand the transmission response of the EIA comprehensively, we introduced various multipoles of scattering power by integrating the scattering current density distribution. The multipole moments are obtained by partial integration of the cell directions  $(\alpha, \beta, \gamma) = (x, y, z)$  [39]:

$$\mathbf{P} = \frac{1}{i\omega} \int \mathbf{J} d^3r \quad (3)$$

$$\mathbf{M} = \frac{1}{2c} \int [\mathbf{r} \times \mathbf{J}] d^3r \quad (4)$$

$$\mathbf{TO} = \frac{1}{10c} \int [(\mathbf{r} \cdot \mathbf{J})\mathbf{r} - 2r^2\mathbf{J}]d^3r \quad (5)$$

$$\mathbf{Q}_{\alpha\beta}^e = \frac{1}{i2\omega} \int \left[ r_{\alpha}j_{\beta} + r_{\beta}j_{\alpha} - \frac{2}{3}(\mathbf{r} \cdot \mathbf{J}) \right] d^3r \quad (6)$$

$$\mathbf{Q}_{\alpha\beta}^m = \frac{1}{3c} \left( \int [(\mathbf{r} \cdot \mathbf{J})_{\alpha}r_{\beta}]d^3r + \{\alpha \leftrightarrow \beta\} \right) \quad (7)$$

where  $\mathbf{P}$ ,  $\mathbf{M}$ ,  $\mathbf{TO}$ ,  $\mathbf{Q}^e$ , and  $\mathbf{Q}^m$  denote electric dipole, magnetic dipole, and toroidal dipole, electric quadrupole, and magnetic quadrupole, respectively, and  $\mathbf{J}$ ,  $\omega$ , and  $c$  denote current density, angular frequency, and speed of light, respectively.

Besides, the scattered power of various multipoles in the far field can be calculated from the polar moments, as shown in Equations (8)–(12) [39]:

$$I_p = \frac{2\omega^4}{3c^3} |\mathbf{P}|^2 \quad (8)$$

$$I_M = \frac{2\omega^4}{3c^3} |\mathbf{M}|^2 \quad (9)$$

$$I_{TO} = \frac{2\omega^4}{3c^3} |\mathbf{TO}|^2 \quad (10)$$

$$I_Q^e = \frac{\omega^6}{3c^5} \sum |Q_{\alpha\beta}^e|^2 \quad (11)$$

$$I_Q^m = \frac{\omega^6}{40c^5} \sum |Q_{\alpha\beta}^m|^2 \quad (12)$$

where  $I_p$ ,  $I_M$ ,  $I_T$ ,  $I_Q^e$ , and  $I_Q^m$  stand for the scattering power of electric dipole, magnetic dipole, toroidal dipole, electric quadrupole and magnetic quadrupole, respectively.

Figure 8 gives the multipole curves for the case of TE waves. The largest contribution is made by the electric dipole  $\mathbf{P}$ , followed by the toroidal dipole  $\mathbf{TO}$ . It can be found that at close to 0.6 THz, at which the scattered power of the toroidal dipole is greater than that of the electric dipole, and the scattered power of all other dipoles is much smaller than that of  $\mathbf{P}$  and  $\mathbf{TO}$ .

### 2.3. The analysis of EIA phenomenon

When the TM wave ( $\theta = 90^\circ$ ) is incident perpendicularly to the MS, the energies of DSR, FSP, and BSP are rearranged. Since the FSR itself has a high symmetry, the sensitivity and response are essentially the same for the TE and TM waves (see Figure 3(c) and Figure 9(c)), and the current flow is still in the direction of the electric field as displayed in Figure 9(d). However, the transmission curves obtained for DSR and BSP are completely different from those for TE waves. In addition, the surface current distribution at 0.615 THz (as shown by the black vector arrow in Figure 9(b)) reveals the electrical resonance triggered by the current in the DSR with a transmission amplitude of 0.028 (particulars shown via Figure 9(a)), indicating the transmission resonant Q-value of 2.06. Moreover, compared with the transmission response for TE waves, it is apparent from Figure 10(a) for TM waves that a strong resonant response can be directly trapped by the incident magnetic field at 0.558 THz with

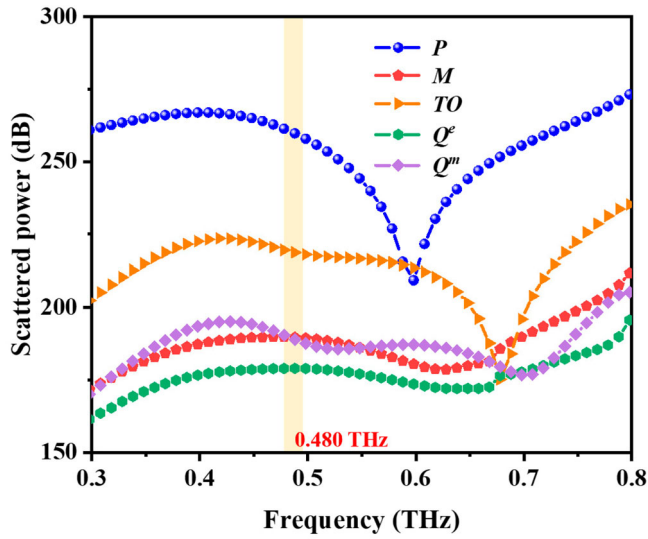


**Figure 8.** The scattered power of different dipoles for EIT.

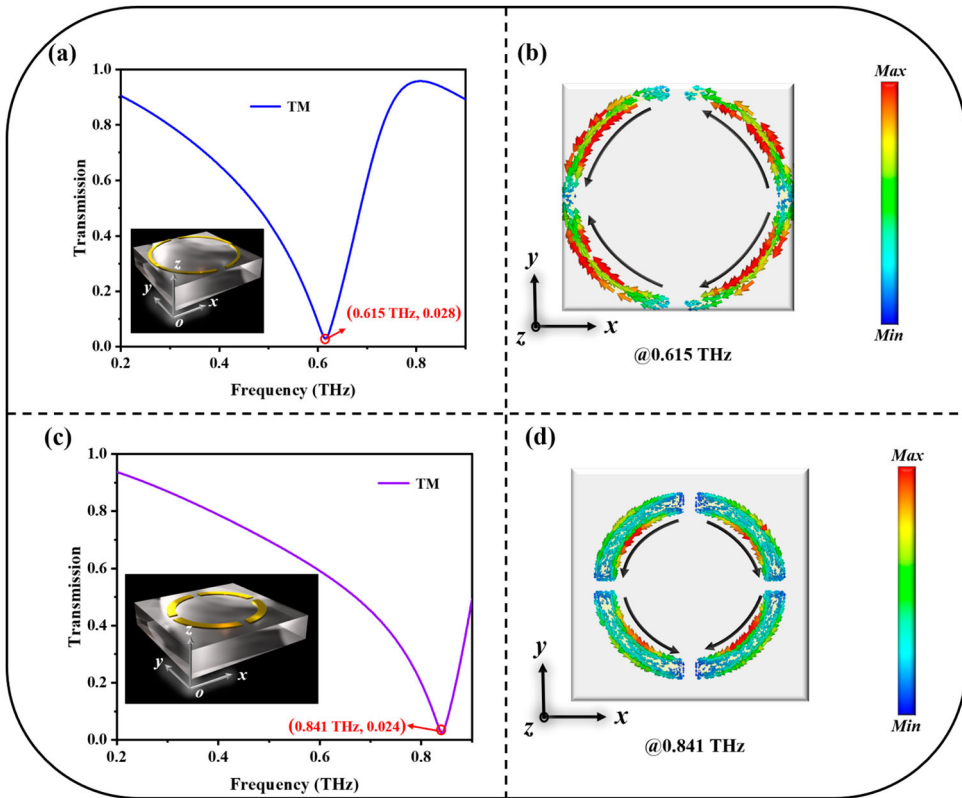


**Figure 9.** With the incidence of TM waves, the transmission response of (a) DSR and (c) FSR, and the corresponding surface current distributions of (b) DSR at 0.615 THz and (d) FSR at 0.841 THz.

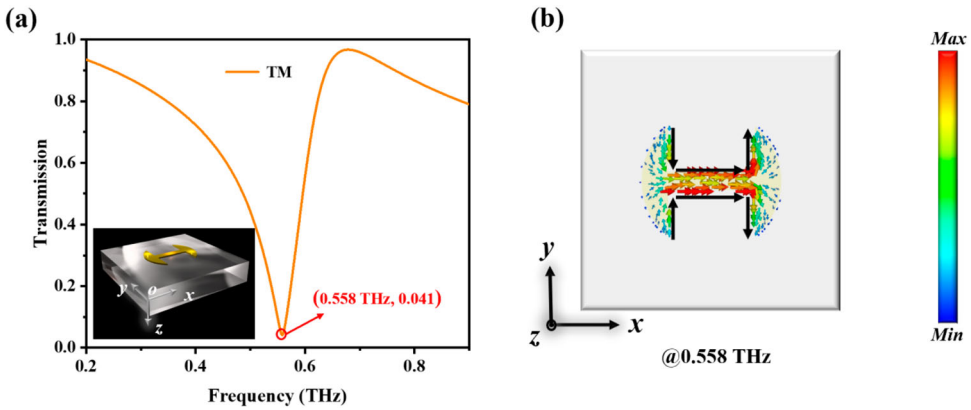


**Figure 10.** (a) Transmission response of BSP under TM wave action and (b) surface current distribution at 0.558 THz.

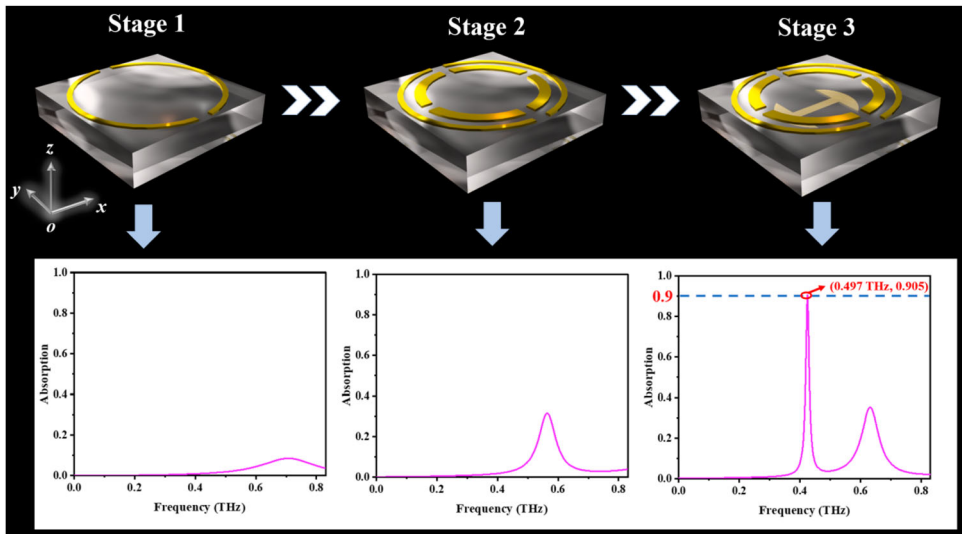


**Figure 11.** The diagrams of the formation process of EIA with the incidence of TM waves.

a transmission amplitude of 0.041, demonstrating that two magnetic dipoles can be formed in the black arrows presented in Figure 10(b).

The MS proposed can achieve the EIA phenomenon for TM waves, which is mainly divided into three main stages as displayed in Figure 11. In stage 1, the DSR can cause a strong phase mutation response. In stage 2, the destructive interference can generate along with the role of FSR due to the near-field coupling. In stage 3, BSP is introduced to produce interlayer magnetic dipoles with significant capture of incident magnetic field energy using three resonant cavities coupled near fields, transforming phase-disrupting interference into phase-constructing interference. Figure 12(a) shows the absorption response of the EIA phenomenon, resulting in the generation of a strong absorption peak at 0.497 THz with an absorption rate of 90.5%. Figure 12(c,d) shows the localization of the energy, reflecting the formation of the absorption peak at 0.497 THz. The surface current distributions (as

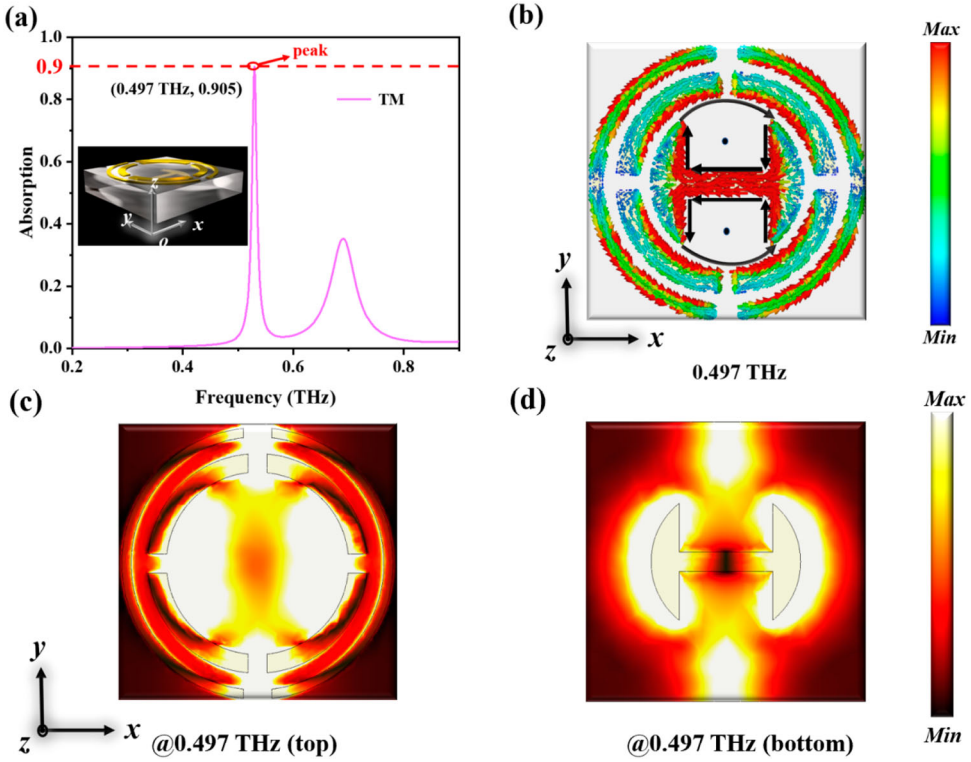


**Figure 12.** (a) The absorption curve of the MS under the action of TM waves, (b) the surface current distribution of the EIA behavior at 0.497 THz, and the electric field distribution (c) for  $z = 10.4 \mu\text{m}$  and (d)  $z = 0 \mu\text{m}$  at 0.497 THz.

exhibited by the black vector arrows in Figure 12(b)) illustrate the appearance of interlayer magnetic dipoles, arising from the phase-constructing interference, thus forming EIA. In addition, the energy states of various dipoles of the EIA have been calculated in this paper through Equations (3)–(12). As can be seen in Figure 13, with a peak near 0.497 THz, the electric dipole scattering dominates the total term of this specific spectrum, where the absorption is the largest. This is mostly caused by the induced electric field that the horizontal oscillator picked up, which produces a strong electrical resonance. It is reassuring to note that the effect of the toroidal dipole **TO** ranks second, while the effect of the other dipoles is weaker. Therefore, the absorption peak is attributed to **P** and **TO**.

#### 2.4. The analysis of LTCPC phenomenon

Since the actual coordinates shift when  $\theta = 45^\circ$ , we no longer use  $x$  and  $y$  to represent the electric and magnetic field directions of the LP wave but use  $u$  and  $v$  instead (see Figure 14(a)). Based on the above derivation, the performance analysis is performed for the given MS. Figure 14(b) depicts the reflection coefficients (main polarized reflection  $R_{uu}$  and cross-polarized reflection  $R_{uv}$ ) and the amplitude variation of the absorbance  $A$ . It can be observed that for the cross-polarized reflected waves, the infinity is close to zero, which is quite substantial for transmitting the LTCPC phenomenon, indicating that most of the LP waves are

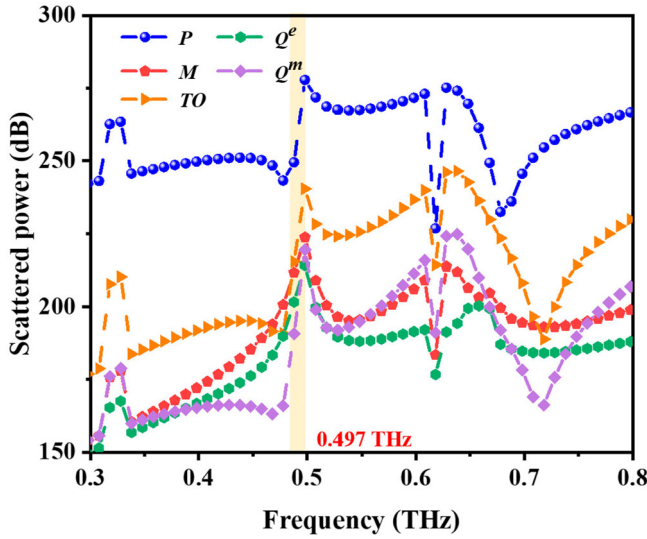


**Figure 13.** The scattered power for different multipoles in MS.

successfully transmitted to the other port. From Figure 14(d), the main polarization transmission ( $T_{uu}$ ) and cross-polarization transmission ( $T_{uv}$ ) curves are given separately, and it can be observed that the ground amplitudes at 0.399 and 0.634 THz are nearly equal, satisfying the amplitude condition for LTCPC. In addition, Figure 14(c,e) provides information on the phase and phase difference, the phase differences of  $-97^\circ$  and  $87.9^\circ$  are very close to the perfect phase condition of the LTCPC. It must be emphasized that the equations are based on ideal lossless conditions; the materials used in the actual design are lossy.

Based on the feasibility study and derivation, the LTCPC phenomenon is investigated with incident  $45^\circ$  LP waves, where the mathematical criterion for LTCPC can be obtained through Equations (13) and (14) [40].

$$T_{uu} = T_{uv} \quad (13)$$

$$\Delta\varphi = \varphi_{uu} - \varphi_{uv} = \frac{\pi}{2} \pm n\pi (n \in Z) \quad (14)$$

where  $\Delta\varphi$  stands for the phase difference. As mentioned in Figure 14, the transmission coefficients at 0.389 THz and 0.634 THz are equal and the corresponding phase differences are nearly  $\pm\pi/2$  for both, satisfying the basic conditions for the occurrence of LTCPC phenomenon.

To determine the performance of the device at different frequencies and polarization states, the transmission axial ratio (AR) of the incident wave LTCPC phenomenon was calculated using the following Equations (15) and (16) [41]:

$$AR = \frac{|T_{uu}|^2 + |T_{uv}|^2 + \sqrt{m}}{|T_{uu}|^2 + |T_{uv}|^2 - \sqrt{m}} \quad (15)$$

$$m = |T_{uu}|^4 + |T_{uv}|^4 + 2|T_{uu}|^2 \cdot |T_{uv}|^2 \cdot \cos(\Delta\varphi) \quad (16)$$

the formation condition of the linear-to-circular polarization transformation and proves the feasibility and correctness of the MS-based LTCPC phenomenon. The circularly polarized

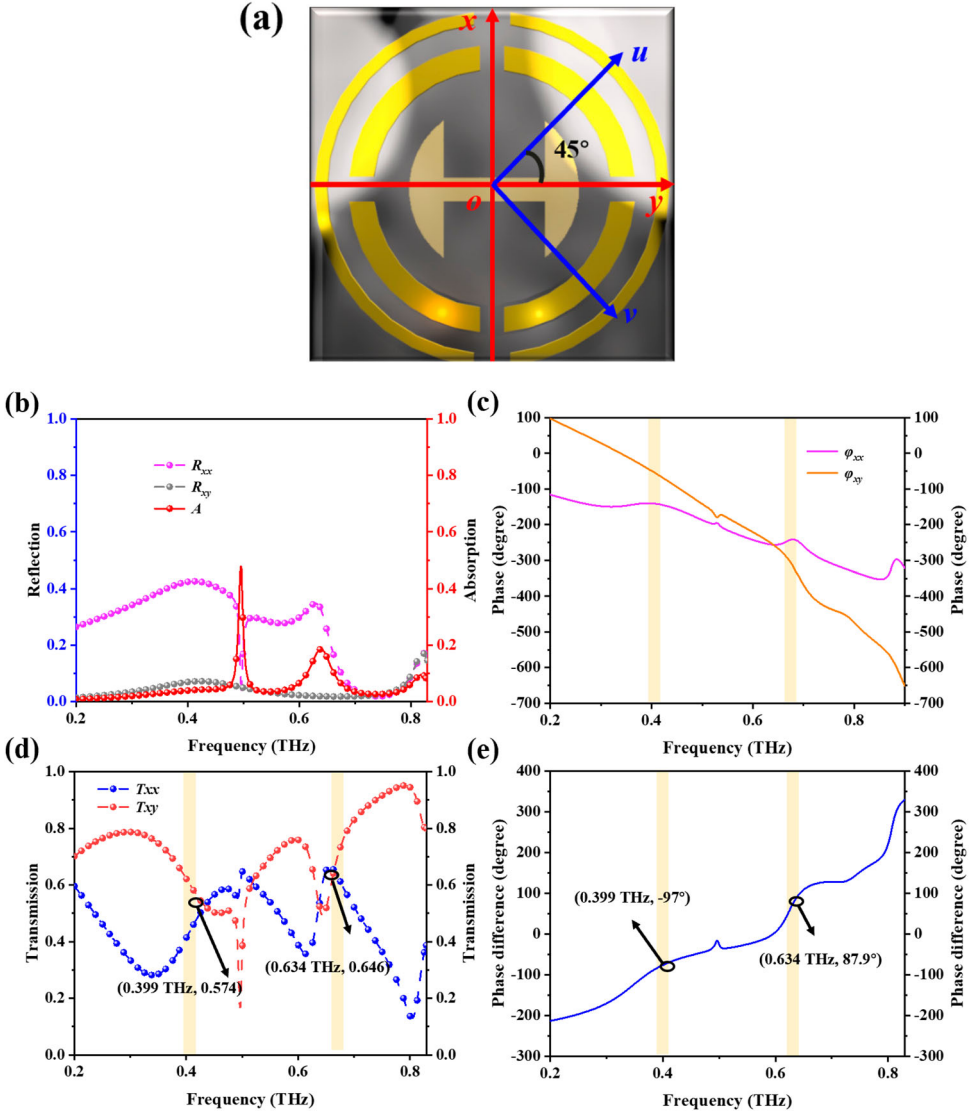


**Figure 14.** When the incident LP wave with  $\theta = 45^\circ$ : (a) Coordinate change demonstration diagram, (b) the corresponding reflective, cross-polarization and absorption curves, (c) the transmission phase of transmissive and transmissive cross-polarization response, (d) interaction points of transmission amplitudes in two polarization modes (0.399 and 0.634 THz) and (e) the calculated phase difference and fluctuation range of the corresponding frequency points.

(CP) waves can be measured by the associated AR less than 3 dB (0.372 THz  $\sim$  0.409 THz and 0.625 THz  $\sim$  0.638 THz). As a result, the 3 dB AR band is calculated as shown in Figure 15(b). The calculated formula of ohm insertion loss (OIL) has shown below [42]:

$$OIL = 1 - |T_{uu}|^2 - |T_{uv}|^2 - |R_{uu}|^2 - |R_{uv}|^2 \quad (17)$$

where the curve of OIL has given in Figure 15(a), demonstrating the low loss of the LTCPC phenomenon (the loss of both 0.399 and 0.634 THz below 0.1). It is worth pointing out that



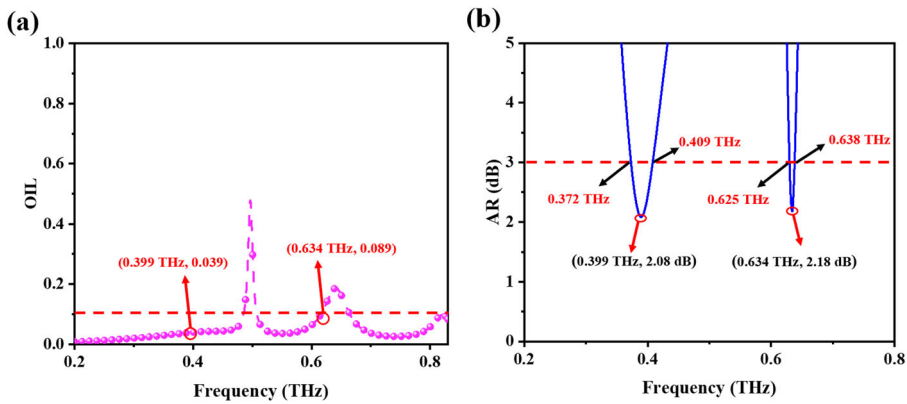


**Figure 15.** (a) Ohm insertion loss and (b) the schematic diagram of the AR of the transmitted LTCPC.

the transmitted light at 0.399 and 0.634 THz can be considered as CP behavior with the transmission amplitude of 0.574 and 0.646, demonstrating the results of low loss. Moreover, the nature of the system is similar to that of a polarizer based on frequency-selective surfaces, while the introduction of EIT and EIA contrasts can successfully achieve the function of phase modulation [43].

Figure 16(a) shows the surface current distribution of the polarization converter designed in this paper at 0.399 THz, and the incident LP wave which it can interact with is  $\theta = 45^\circ$  relative to both  $x$ - and  $y$ -axis directions, whose electric field vector is  $E_{in}$ . Assuming that the currents generated on the DSR are  $I_{D1}$  and  $I_{D2}$ , and on the BSP is  $I_B$ , the current synthesis of these three can induce the electric field  $E_i$ , and  $E_i$  can vector decomposition into an electric field  $E$  with a phase difference of  $90^\circ$  from the incident electric field and equal amplitude, satisfying the formation condition of LTCPC. A similar principle of the LTCPC phenomenon can be formed at 0.634 THz. As can be seen in Figure 16(b), the DSR

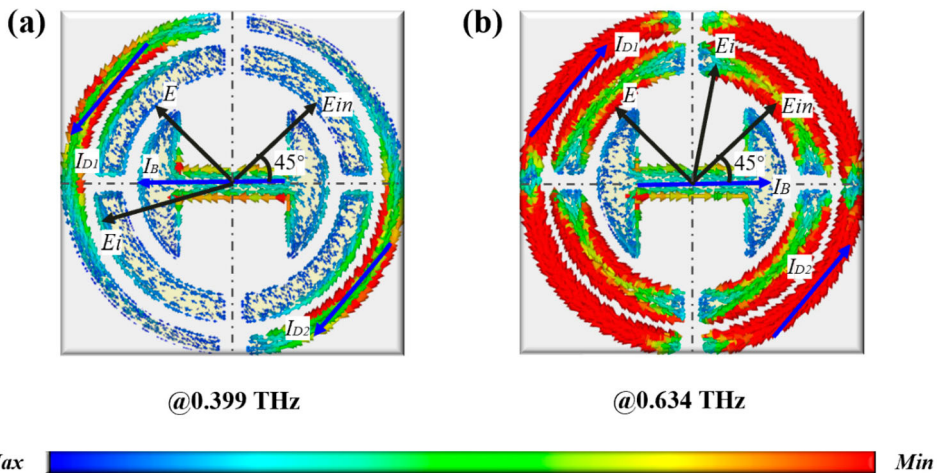


**Figure 16.** The surface current distribution of MS at (a) 0.399 THz and at (b) 0.634 THz.

and FSR currents flow in opposite directions and both appear strongly coupled to the incident wave. However, the opposite flow direction indirectly leads to the fact that most of the energy can cancel each other in the  $z$ -axis. Since the electric field energy on the DSR is larger than that on the FSR, the DSR retains the energy and forms the induced electric field  $E$  together with the current  $I_B$  on the BSP, which can still form the LTCPC condition with equal amplitude and  $90^\circ$  phase difference with the incident electric field by vector decomposition. Although somewhat more complicated to handle, can be applied to radomes and information encryption devices and channel multiplexing [44,45], also greatly avoiding the limitations of reflection geometry and interference [46].

## 2.5. Quantum system theory of EIT and EIA

For further understanding of the mechanism of EIT and EIA behaviors in this MS, as demonstrated in Figure 17, since interference between two different stimulus paths can achieve both EIT and EIA behavior, a three-energy atomic system has been introduced here [35], where  $\gamma_1$  and  $\gamma_2$  are the coupling coefficients between energy levels, and  $\Omega_1$  and  $\Omega_2$  denote the transition phase.  $p$  is the coupling coefficient between levels  $|1\rangle$  and  $|3\rangle$ . It is obvious from Figure 17 that two energy transition channels are created from the ground state energy level  $|1\rangle$  to the excited state energy level  $|2\rangle$  and from the excited state energy level  $|2\rangle$  to the other ground state energy level  $|3\rangle$ . The excitement can almost entirely absorb the probing light. The transmission channel between  $|1\rangle$  and  $|3\rangle$  is disabled. Furthermore, when the external electromagnetic field can guide the atoms in  $|1\rangle$  to leap to  $|2\rangle$ , and the atoms in the  $|2\rangle$  energy level are in an excited unstable state, the atoms automatically leap to  $|3\rangle$ , and with the addition of the coupling light, the atoms in the  $|3\rangle$  energy level are excited back to  $|2\rangle$  again, thus forming two channels ( $|1\rangle \rightarrow |2\rangle$  and  $|1\rangle \rightarrow |2\rangle \rightarrow |3\rangle \rightarrow |2\rangle$ ). Thanks to the destructive interference in the transition channel, a significant EIT window is obtained. The EIT behavior can be produced in the proposed MS by the destructive interference of two bright resonant cavities, which can be analogous to the EIT phenomenon of a MS for TE waves.

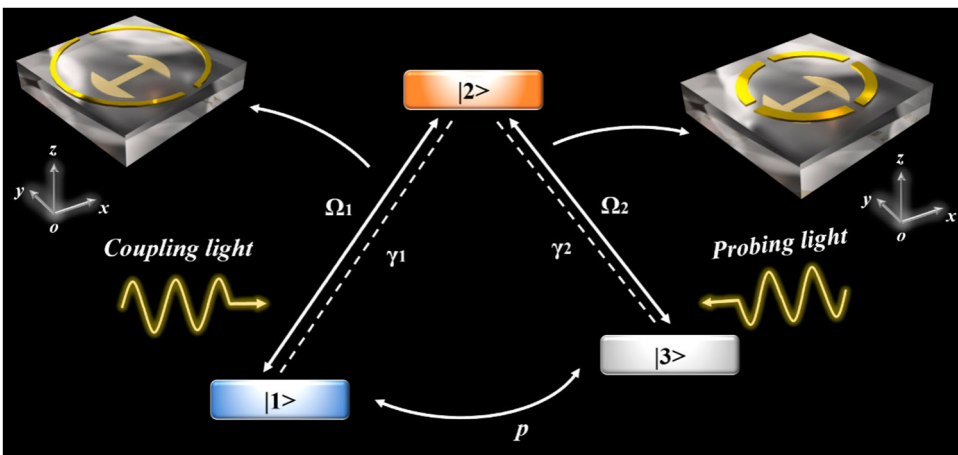


**Figure 17.** Theoretical analysis of the three atomic levels of EIT and EIA.

A three-atomic level system with characteristics similar to that of the EIT can also be used to elucidate the coupling mechanism of the EIA system. EIA or EIT effects can be formed between two different channels characterizing two modes. The EIT behavior (BSP does not couple with TE waves) can evolve into EIA behavior (BSP couples with TM waves) if the form of interference between the two paths changes from destructive to constructive. In the radiation resonant oscillator model, the coupling between the attenuated radiation modes can convert the EIT behavior into EIA behavior effectively (can be seen as the role of the BSP in the MS), which is equivalent to the introduction of coupled phase detuning (i.e.  $p(\varphi) = pe^{i\varphi}$ ). To advance the self-modulation properties of this MS system, a polarization-sensitive system is on the agenda, where the excitation of the BSP for TM waves offers the energy localization of the dual bright-mode system a coupling channel, boosting the BSP dissipation to the bright mode. The generated constructive interference overwhelms the residual coherent dissipation effect, further causing the high absorption in the frequency band of original transparent window, indirectly weakening the destructive interference effect.

### 3. Theoretical models of EIT and EIA effects

#### 3.1. Two-oscillator model

Under the EIT behavior, the BSP can be ignored because it cannot couple with the incident TE waves. The two-oscillator model can be used to quantitatively describe the interaction of the double bright modes, which can be expressed by the following equation [47,48]:

$$\ddot{x}_1(t) + \gamma_1 \dot{x}_1(t) + \omega_0^2 x_1(t) + \zeta^2 x_2(t) = g_1 E(t) \quad (18)$$

$$\ddot{x}_2(t) + \gamma_2 \dot{x}_2(t) + (\omega_0 + \delta)^2 x_2(t) + \zeta^2 x_1(t) = g_2 E(t) \quad (19)$$

where  $x_1(t)$  and  $x_2(t)$  denote the displacements of the two bright oscillators (DSP and FSR) irradiated by the induced electric field  $E(t) = E_0 e^{i\omega t}$ , respectively, interacting directly with the two bright oscillators ( $x_1(t)$  and  $x_2(t)$ ) through the coupling coefficient  $g_1$  and  $g_2$ . The detuning coefficient between the oscillator transparent frequency and the intrinsic frequency is represented by  $\delta$ .  $\gamma_1$ ,  $\gamma_2$ , and  $\zeta$  correspond to the oscillation damping and the coupling strength between the two oscillators, respectively. To facilitate the calculation, the value of  $g_2$  is set to 0. Supposing  $x_1(t) = x_1 e^{i\omega t}$ ,  $x_2(t) = x_2 e^{i\omega t}$ ,  $\omega_1^2 - \omega^2 \approx 2\omega_1(\omega_1 - \omega)$ , the transmission formula can be obtained [47,48]:

$$T = 1 - \text{Re} \frac{ig^2(\omega - \omega_0 - \delta - i\gamma_2)}{(\omega - \omega_0 + i\gamma_1/2)(\omega - \omega_0 - \delta + i\gamma_2/2) - i\zeta^2/4} \quad (20)$$

$T$  is the transmissibility and the key fitted parameters are:  $\gamma_1 = 2.06$ ,  $\gamma_2 = 1$ ,  $\omega_0 = 3.8$  with the incidence of TE waves.  $\text{Re}()$  donates taking the real part. The corresponding transmission curves of simulation and calculation have exhibited in Figure 18(a).  $\gamma_1 > \gamma_2$  (TE waves) shows the large radiation loss of the directly excited DSR here. The errors in the approximation and number of iterations of the calculated equations and transmission losses in Figure 18(a) and the neglect of the minor role of BSP in the theoretical simulations make the theoretical results inevitably show tolerable differences compared to the simulated results. Nevertheless, the physical mechanism of the EIT can still be reflected quite graphically in the mechanical two-oscillator model.

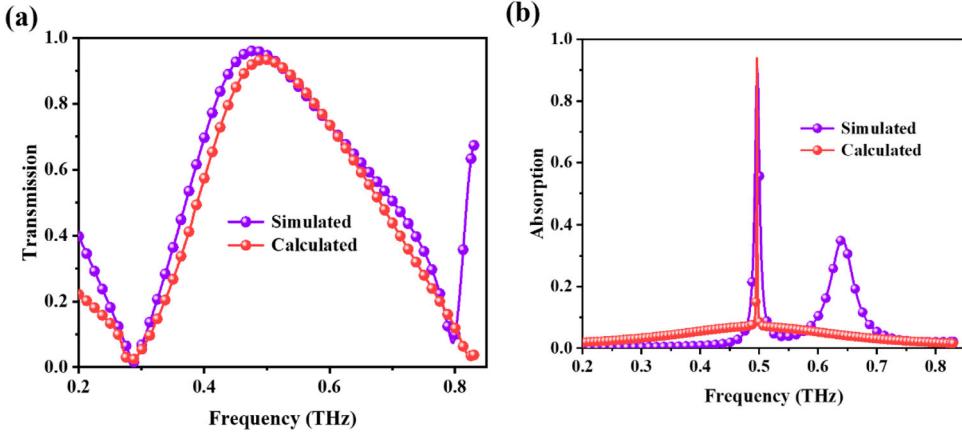


**Figure 18.** Comparison of theoretical transmission curves and simulation curves of (a) EIT and (b) EIA.

When the TM wave irradiating the MS induces the BSP to function, the transmitted light energy is captured by the magnetic dipole between the layers, producing an energy localization effect and a violent enhancement of the current on the resonator. The two-oscillator model of EIA is based on EIT, the DSR, and FSR are considered together as one oscillator and the BSP as the other oscillator in the simulation of EIA. Since the change from destructive to constructive interference involves a phase difference of  $\pi/2$ , the interference term of the coupling strength is of the complex form  $\zeta(\Phi) = \zeta e^{j\Phi}$ . The two-oscillator model expression of quantitative analysis is changed into formulas as shown below [47,48]:

$$\ddot{x}_1(t) + \gamma_1 \dot{x}_1(t) + \omega_0^2 x_1(t) + \zeta e^{j\Phi} x_2(t) = g_1 E(t) \quad (21)$$

$$\ddot{x}_2(t) + \gamma_2 \dot{x}_2(t) + (\omega_0 + \delta)^2 x_2(t) + \zeta e^{j\Phi} x_1(t) = 0 \quad (22)$$

The constructive interference in the coupling process triggers the EIA, which is manifested by the absorption  $A$  [47,48]:

$$A = \text{Re} \frac{ig_1^2(\omega - \omega_0 - \delta + i\gamma_2/2)}{(\omega - \omega_0 + i\gamma_1/2)(\omega - \omega_0 - \delta + i\gamma_2/2) - \zeta^2 e^{i2\Phi}/4} \quad (23)$$

The key parameters for theoretical fitting of EIA for TM waves are:  $\gamma_1 = 2.2$ ,  $\gamma_2 = 0.1$ ,  $\omega_0 = 3.12$ . Because BSP has a strong ability to capture the magnetic field and produces a high absorption effect, the fitting trend shift can be observed in the case of dual-mode incidence (more obvious in Figure 18(b)). Comparing the key physical quantity (EIA effect) with the physical quantity in the EIT state, the dissipation loss of EIA ( $\gamma_1$ ) is far greater than the dissipation loss of radiation mode. The increase of  $\gamma_1$  corresponds to DSR resonance in EIA. However, the relationship under EIA status  $\gamma_1$  and  $\gamma_2$  (compared with the  $\gamma_1$  and  $\gamma_2$ ). The change in coupling strength modulus value indicates that there is residual failure coupling, which is equivalent to the linear low transmission of residual EIT. The dominant absorption is obtained from the structural inference, and the EIA effect is obtained. The reason for the difference between the theoretical absorption curve and the simulation curve can be attributed to the local energy of the surface magnetic dipole that may be formed between BSP and FSR, resulting in the appearance of a small peak in the absorption curve as shown in Figure 18(b), but has no impact on the overall performance.

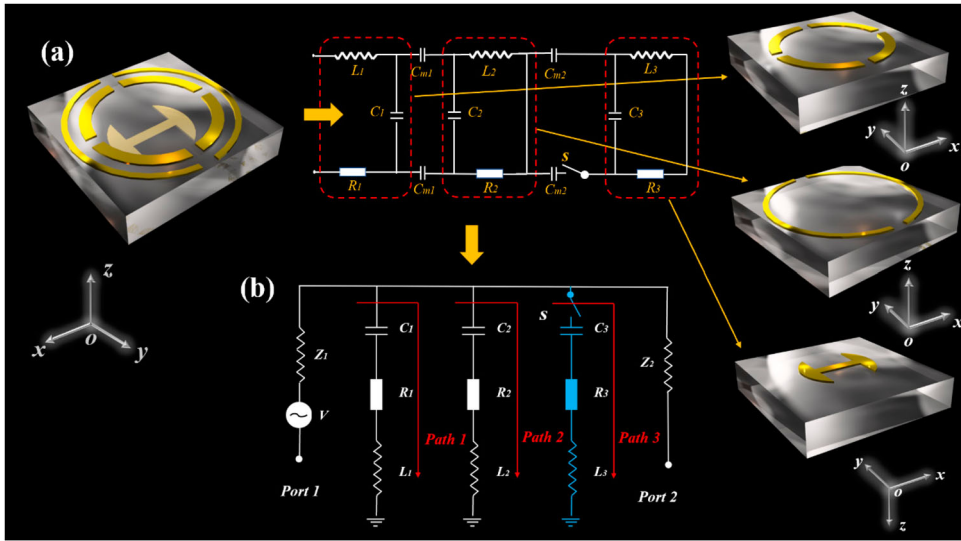


**Figure 19.** (a) Circuit equivalence diagram of DSP, FSR and BSP, (b) Circuit equivalents of EIT and EIA.

### 3.2. Equivalent RLC circuit model

Here, the equivalent circuit of the MS will be analyzed qualitatively [49,50]. It can be found that the DSR and FSR in the proposed MS can be represented by two resonant circuits respectively (as shown in Figure 19(a)), where  $L_1$  is the self-inductance of FSR,  $C_1$  is the gap capacitance of FSR, and  $R_1$  is the resistance (the resistance is the loss, including ohmic loss and radiation loss). Similarly, the self-inductance, gap capacitance, and resistance of DSR (BSP) are expressed by  $L_2(L_3)$ ,  $C_2$  ( $C_3$ ), and  $R_2$  ( $R_3$ ), respectively [51]. Since the BSP structure only works under TM irradiation and the BSP structure is mainly used to enhance DSR and FSR losses, the formation mechanism of EIT and EIA is still determined by the coupling path between DSR and FSR, so the third resonant loop which stands for BSP uses the switch  $k$  to characterize the conversion of EIT and EIA for TE and TM waves. The source impedance  $Z$  on port 1 and port 2 can be changed to enhance the losses to achieve the transition from destructive interference to constructive interference (and vice versa). In addition, the coupling capacitances  $C_{m1}$  and  $C_{m2}$  are used to reflect the coupling effect between DSR, FSR, and BSP. The equivalent circuit of the MS is shown in Figure 19(b). Under TE wave irradiation, the BSP does not play a role and the switch  $s$  is disconnected, while the DSR and FSR actions represent two coupling paths (path 1 and 2), respectively.

As exhibited in Figure 20(a), once the two paths are combined ( $s$  is unconnected), they can open a transparent window in an opaque section of the spectrum, forming a destructive interference phenomenon with slow light effects (EIT). The theoretical and simulated curves of the EIT phenomenon basically coincide, but there is a small error, which can be attributed to the neglect of the small interference of the BSP for the TE wave and the refraction of the most incident waves from the dielectric substrate during the circuit simulation. The comparison plots of the final theoretical and simulated curves are given in Figure 20(b). Similarly, when the source impedance  $Z$  between the ports is changed and the switch  $s$  is connected, the loss can be enhanced between the interference paths, which can greatly offset the

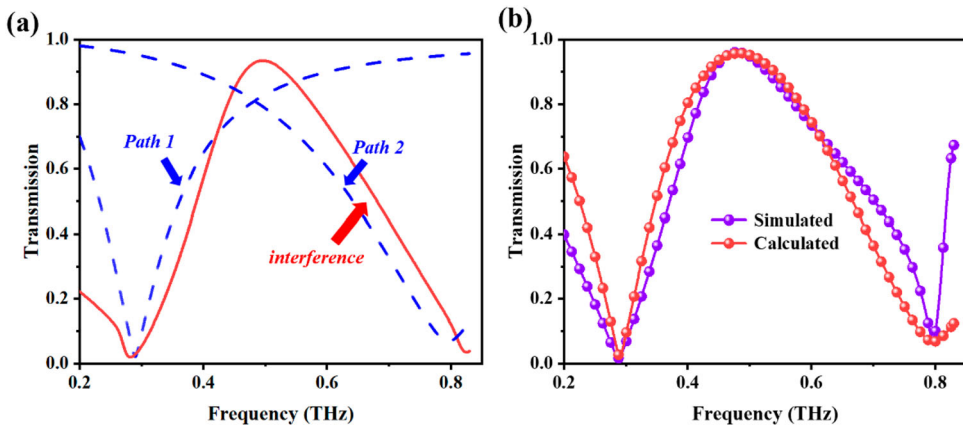


**Figure 20.** (a) Theoretical process of circuit fitting, (b) comparison of theoretical and simulated curves of EIT for TE waves.

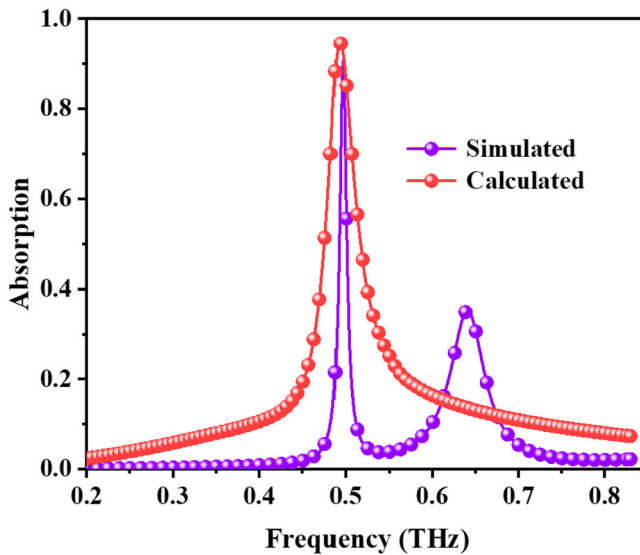


**Figure 21.** The comparison diagram of simulated and calculated curves in EIA for TM waves.

effect of destructive interference and induce the appearance of constructive interference, thus forming the EIA phenomenon (see Figure 21). A certain discrepancy between the theoretical and actual EIA curves is attributed to the ability of the DSR and FSR to form a magnetic dipole between them, and the energy of the local magnetic field, making a small peak of absorption on the right side, which has a negligible impact on the overall MS performance and can therefore be ignored. Besides, neglecting the coupling capacitance and inductance effect between each series loop in the circuit simulation is also the main reason for the error between the simulation and the theoretical curve. The individual key parameters for the actual EIT and EIA circuit simulations will be given in Tables 2 and 3.

**Table 2.** The key parameters of EIT phenomenon.

Parameters	Value	Parameters	Value
$R_1$	$0.5 \Omega$	$R_2$	$1.8 \Omega$
$L_1$	$18 \text{ pH}$	$L_2$	$7 \text{ pH}$
$C_1$	$16.7 \text{ fF}$	$C_2$	$5.65 \text{ fF}$
$Z_1$	$50 \Omega$	$Z_2$	$50 \Omega$

**Table 3.** The key parameters of EIA phenomenon.

Parameters	Value	Parameters	Value
$R_1$	$2 \Omega$	$R_3$	$1 \Omega$
$L_1$	$18 \text{ pH}$	$L_3$	$6.3 \text{ pH}$
$C_1$	$4.5 \text{ fF}$	$C_3$	$13 \text{ fF}$
$R_2$	$0.5 \Omega$	$Z_1$	$10 \Omega$
$L_2$	$7 \text{ pH}$	$Z_2$	$300 \Omega$
$C_2$	$18 \text{ fF}$		

#### 4. The parameters discussion

To further investigate the effect of MS geometrical parameters on the performance of EIT, EIA, and LTCPC, the difference between the inner and outer diameters  $w_1$  of DSR and the arm length  $a$  of BSP are specifically selected for discussion. Figure 22 clearly shows the EIT and EIA behaviors of  $w_1$  for TE and TM waves in the isometric range between 3 and 7  $\mu\text{m}$  and the LTCPC phenomenon when  $\theta = 45^\circ$ . As  $w_1$  increases, the coordinates of the peaks corresponding to EIT are (0.444 THz, 0.950), (0.480 THz, 0.961), (0.477 THz, 0.948), and (0.491 THz, 0.939), while the coordinates of the peaks corresponding to EIA are (0.472 THz, 0.871), (0.497 THz, 0.905), (0.472 THz, 0.887) and (0.471 THz, 0.897). Since  $w_1$  greatly affects the energy distribution of DSR, it is very obvious that EIT, EIA, and LTCPC behaviors exhibit offset phenomena for different PAs. As  $w_1$  increases, the coordinates of the two AR nadir points are: (0.357 THz, 1.92 dB), (0.399 THz, 2.08 dB), (0.401 THz, 3.27 dB), (0.411 THz, 3.90 dB) and (0.601 THz, 2.25 dB), (0.634 THz, 2.18 dB), (0.620 THz, 2.19 dB), (0.630 THz, 3.04 dB), respectively. However, it can be observed in Figure 22(c) that the AR of LTCPC phenomenon satisfies the requirement of less than 3 dB when the values of  $w_1$  are 3 and 5  $\mu\text{m}$ . Not only that, as shown in Figure 22(a), only when  $w_1$  is at 5  $\mu\text{m}$ , the two transmission valleys of EIT can reach the minimum (less than 0.1). For the EIA phenomenon, the absorption peak reaches its highest at  $w_1$  of 5  $\mu\text{m}$ , and the incident magnetic energy in the interlayer magnetic dipole is the strongest, and can best reduce the energy of the incident magnetic field energy in the local area of the surface magnetic dipole formed between DSR and FSR. The absorption response curve (see Figure 22(b)) shows well that at  $w_1 = 5 \mu\text{m}$ , the right absorption peak is the lowest and the EIA peak is the highest. Therefore, for the geometrical parameter  $w_1$ , 5  $\mu\text{m}$  is the best choice.

Additionally, we have selected the arm length  $a$  (48  $\mu\text{m} \sim 52 \mu\text{m}$ ) of the geometric parameter BSP in Figure 23 for discussion. For the EIT phenomenon (see Figure 23(a)), it is found that the variation of  $a$  in this interval does not change the EIT performance much. Only when  $a = 50 \mu\text{m}$ , the EIT transmission response undergoes a more pronounced blue shift, and the second transmission valley of the EIT reaches the lowest and best performance. Similarly, for the AR of LTCPC, the reason for choosing 50  $\mu\text{m}$  is to sacrifice the tiny

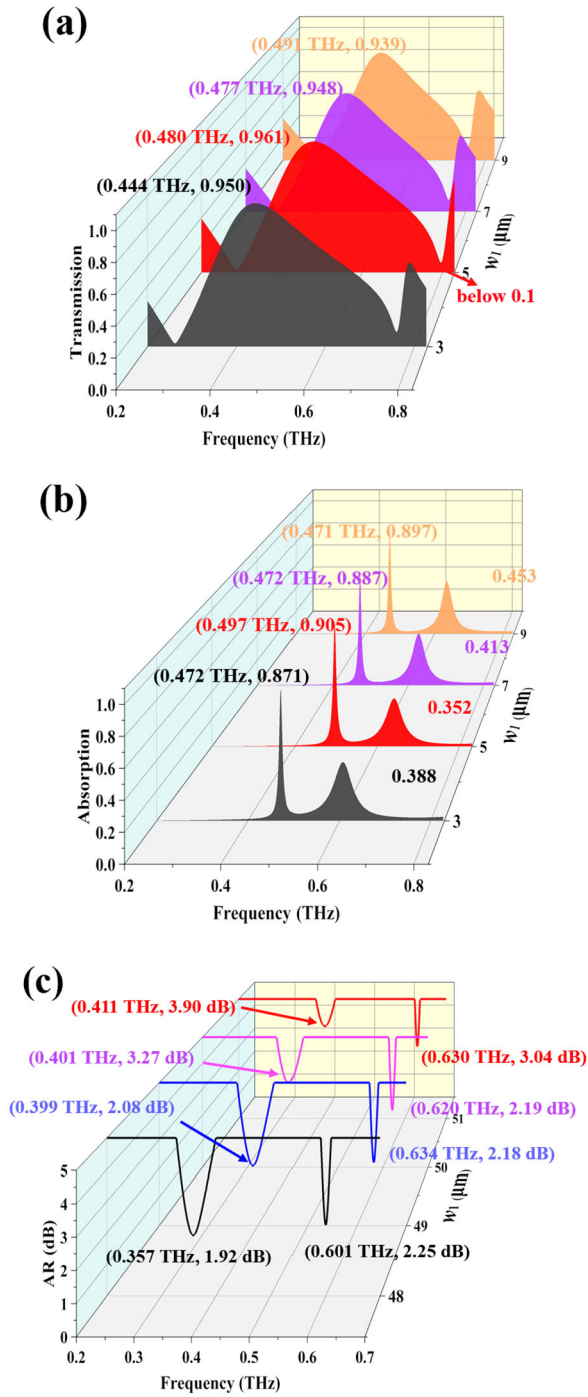


**Figure 22.** The discussion of the key parameter  $w_1$  ranging from 3 to 7  $\mu\text{m}$  for (a) EIT, (b) EIA and (c) LTCPC phenomenon.



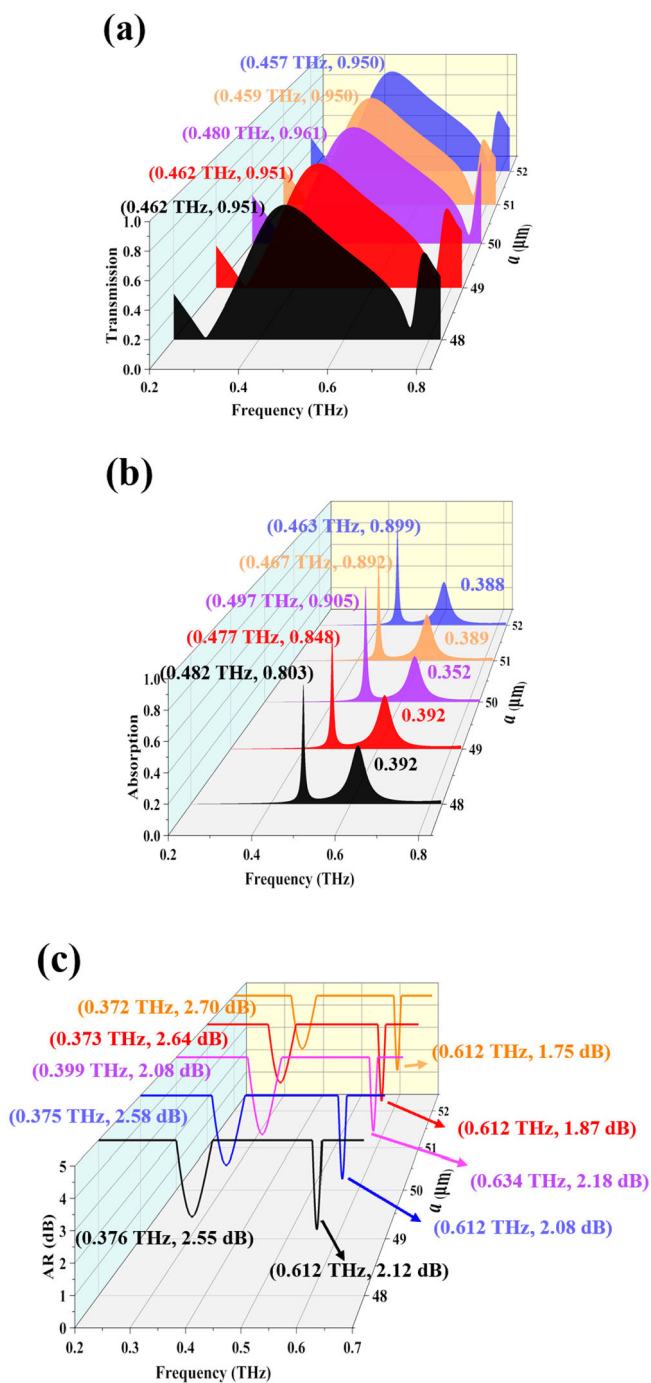


**Figure 23.** Discussion of the results for important parameters  $a$  ranging from 48 to 52  $\mu\text{m}$  for (a) EIT, (b) EIA and (c) LTCPC phenomenon.

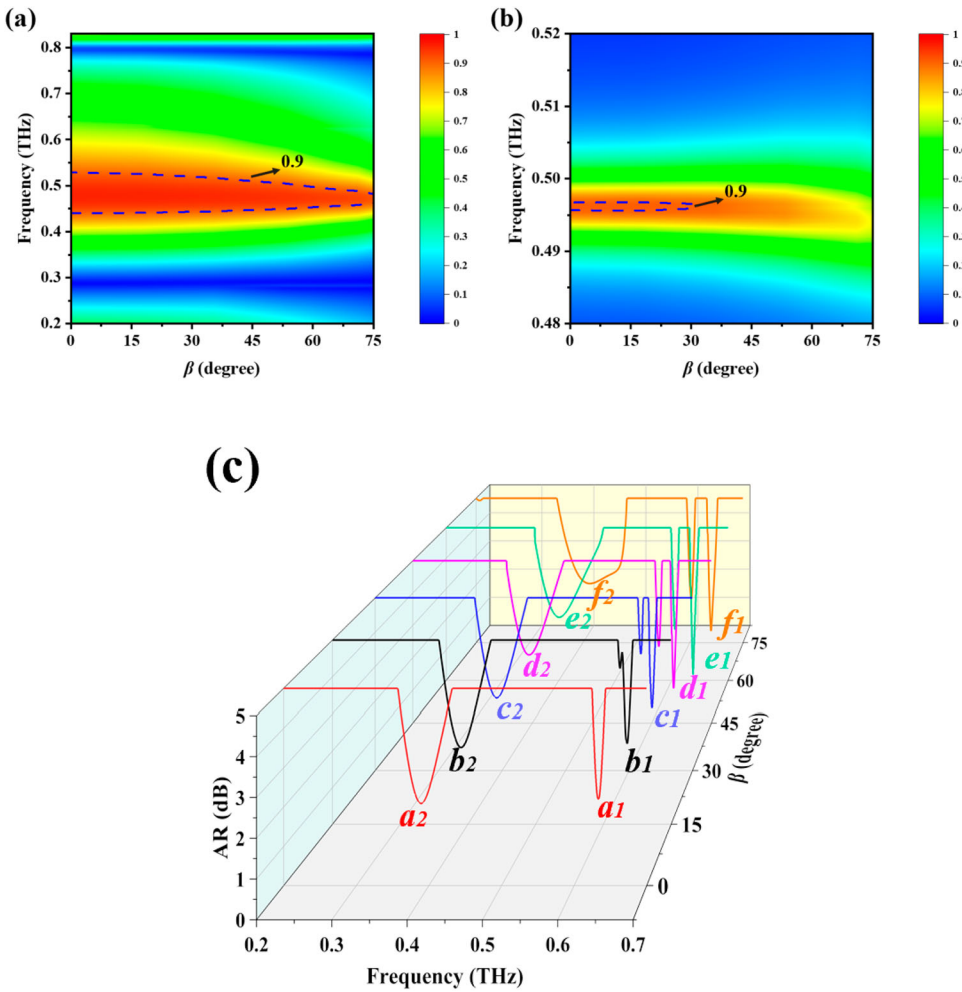


**Figure 24.** The transmission (a), the absorption (b) and the ARs (c) at different incident angle ( $\beta$  varies from  $0^\circ$  to  $75^\circ$ ).

AR of the right polarization conversion frequency point to achieve better polarization conversion on the left side, as shown in Figure 23(c). With the increment of  $a$ , the coordinates of the two AR nadir points are: (0.376 THz, 2.55 dB), (0.375 THz, 2.58 dB), (0.399 THz, 2.08 dB), (0.373 THz, 2.64 dB), (0.372 THz, 2.70 dB) and (0.612 THz, 2.12 dB), (0.612 THz, 2.08 dB), (0.634 THz, 2.18 dB), (0.612 THz, 1.87 dB), (0.612 THz, 1.75 dB), respectively. The change of parameter  $a$  has a large impact on the performance of the EIA for TM waves as exhibited in Figure 23(b). It can be found that, except for  $a = 50 \mu\text{m}$ , the absorption curve undergoes a more pronounced red shift with increasing  $a$  and the peak increases gradually. Once the value of  $a$  reaches  $50 \mu\text{m}$ , the whole absorption curve undergoes a larger blue shift and can effectively reduce the effect of the small peak point of the right absorption, which can be attributed to the fact that the energy localization of the interlayer magnetic dipole at  $a$  at  $50 \mu\text{m}$  indirectly enhances the energy loss of the DSR, thus enhancing the EIA and weakening the magnetic

**Table 4.** Functional overview of polarization-angle-related MS.

PA	Phenomenon	Performance
0°	EIT	0.441 THz ~ 0.531 THz ( $T \geq 0.9$ )
45°	LTCPC	0.372 THz ~ 0.409 and 0.625 THz ~ 0.638 THz ( $AR \leq 3$ dB)
90°	EIA	0.497 THz ( $A \geq 0.9$ )

**Table 5.** The comparison of previous work.

Reference	Frequency regime	EIT	EIA	LTCPC	PA controlled
[52]	0.4–1.8 THz	NO	NO	YES	NO
[22]	0.5–0.9 THz	YES	YES	NO	NO
[31]	0.7–1.5 THz	YES	NO	YES	YES
[35]	1.2–1.5 THz	YES	YES	YES	NO
This paper	0.2–0.9 THz	YES	YES	YES	YES

energy of the small magnetic dipole between the DSR and FSR. As  $a$  increases, the coordinates of the peaks corresponding to EIT are (0.462 THz, 0.951), (0.462 THz, 0.951), (0.480 THz, 0.961), (0.459 THz, 0.950) and (0.457 THz, 0.950), while the coordinates of the peaks corresponding to EIA are (0.482 THz, 0.803), (0.477 THz, 0.848), (0.497 THz, 0.905), (0.467 THz, 0.892) and (0.463 THz, 0.899).

In summary,  $w_1 = 5 \mu\text{m}$  and  $a = 50 \mu\text{m}$  are optimal. The MS based on LTCPC proposed in this paper opens up possibilities for applications in the field of PA control and antennas.

In addition to the discussion of the geometric parameters, the incident angle ( $\beta$ ) is also analyzed in this paper. The variation of transmission ( $\theta = 0^\circ$ ), absorption ( $\theta = 90^\circ$ ), and AR ( $\theta = 45^\circ$ ) with the incidence angle is given in Figure 24. From Figure 24(a), it can be obtained that the overall performance of the EIT has little effect as the incidence angle increases, but the bandwidth decreases accordingly. Figure 24(b) provides the absorption near the EIA absorption peak frequency point of 0.497 THz when  $\beta = 90^\circ$ . The absorption at 0.497 THz is still in a strong state until  $\beta = 30^\circ$ , but once  $\beta \geq 30^\circ$ , the absorption amplitude decreases considerably. The coordinates of  $a_2 \sim f_2$  in Figure 24(c) are (0.399 THz, 2.08 dB), (0.389 THz, 2.09 dB), (0.391 THz, 2.09 dB), (0.392 THz, 2.10 dB), (0.400 THz, 2.06 dB), (0.416 THz, 2.05 dB) and  $a_1 \sim f_1$  are: (0.634 THz, 2.18 dB), (0.635 THz, 2.20 dB), (0.636 THz, 1.78 dB), (0.636 THz, 1.05 dB), (0.637 THz, 0.18 dB), (0.640 THz, 0.41 dB), respectively. It is worth noting that the angle of incidence has very little effect on the overall performance of the LTCPC phenomenon, and can even be improved to a certain extent, with the AR at  $60^\circ$  and  $75^\circ$  already below 0.5 dB as exhibited in Figure 24(c), allowing for a more perfect CP wave. In conclusion, the functionality of the proposed device is stable within an incidence angle of  $45^\circ$ , which has great potential applications in the fields of sensors, antennas, etc.

## 5. Conclusion

In this paper, a multitasking MS related to PA has been proposed in the THz range (See Table 4). Different PAs of LP waves can trigger different functions. The incidence of TE waves ( $\theta = 0^\circ$ ) enables EIT, while EIA can be induced for TM waves ( $\theta = 90^\circ$ ). Under the incidence of TE waves, the transparency window of EIT can be obtained from 0.288 THz to 0.797 THz accompanied by a slow light effect with a relative bandwidth of 18.5%, satisfying the requirement of broadband EIT. The maximum GD reaches 2.51 ps, corresponding

to a GI of 72.5. For TM waves, the EIA can be obtained which has an absorption peak of 0.497 THz. When  $\theta = 45^\circ$ , the LTCPC phenomenon is obtained at 0.389 THz and 0.634 THz, where the transmission coefficients are as high as 0.571 and 0.650 with less loss. the lowest ARs of LTCPC are 2.08 dB at 0.389 THz and 2.18 dB at 0.634 THz, respectively. It is worth noting that the two-oscillator and circuit models analyze EIT and EIA theoretically, and the conclusions obtained were in general agreement with the simulation results. More importantly, the proposed MS has a large polarization selectivity for electromagnetic waves. Thus, the multitasking MS proposed goes beyond the conventional MSs, and possesses all three properties simultaneously controlled by PA, which provides a new way to manipulate the properties of electromagnetic waves, and can be applied to PA control devices, antenna fields, and wave plate integration. To better illustrate the novelty of the paper, we have compared previous works with the paper as displayed in Table 5.

## Disclosure statement

No potential conflict of interest was reported by the author(s).

## Funding

This work was supported by the National College Student Innovation Training Program [grant number 202210293014Z], and College Student Innovation Training Program of Nanjing University of Posts and Telecommunications.

## References

- [1] Kim JY, Soref R, Buchwald WR. Multi-peak electromagnetically induced transparency (EIT)-like transmission from bull's-eye-shaped metamaterial. *Opt Express*. 2010;18(17):17997–18002.
- [2] Boller KJ, Imamoğlu A, Harris SE. Observation of electromagnetically induced transparency. *Phys Rev Lett*. 1991;66(20):2593–2596.
- [3] Totsuka K, Kobayashi N, Tomita M. Slow light in coupled-resonator induced transparency. *Phys Rev Lett*. 2007;98(21):213904.
- [4] Baba T. Slow light in photonic crystals. *Nat Photonics*. 2008;2(8):465–473.
- [5] Zhang S, Genov DA, Wang Y, et al. Plasmon-Induced transparency in metamaterials. *Phys Rev Lett*. 2008;101(4):047401.
- [6] Hung YH, Cheng QX, Glick M, et al. Silicon photonic switch-based optical equalization for mitigating pulsewidth distortion. *Opt Express*. 2019;27(14):19426–19435.
- [7] Shinada S, Furukawa H, Wada N. Huge capacity optical packet switching and buffering. *Opt Express*. 2011;19(26):B406–B414.
- [8] Harris SE, Field JE, Imamoglu A. Nonlinear optical processes using electromagnetically induced transparency. *Phys Rev Lett*. 1990;64(10):1107–1110.
- [9] Guo Y, Yan L, Pan W, et al. Electromagnetically induced transparency (EIT)-like transmission in side-coupled complementary split-ring resonators. *Opt Express*. 2012;20(22):24348–24355.
- [10] Pu M, Hu C, Huang C, et al. Investigation of fano resonance in planar metamaterial with perturbed periodicity. *Opt Express*. 2013;21(1):992–1001.
- [11] Singh R, Rockstuhl C, Lederer F, et al. Coupling between a dark and a bright eigenmode in a terahertz metamaterial. *Phys Rev B*. 2009;79(8):08511.
- [12] Lu Y, Rhee JY, Jang WH, et al. Active manipulation of plasmonic electromagnetically-induced transparency based on magnetic plasmon resonance. *Opt Express*. 2010;18(20):20912–20917.
- [13] Bai Q, Liu C, Chen J, et al. Tunable slow light in semiconductor metamaterial in a broad terahertz regime. *J Appl Phys*. 2010;107(9):093104–093108.
- [14] Jin XR, Park J, Zheng HY, et al. Highly-dispersive transparency at optical frequencies in planar metamaterials based on two-bright-mode coupling. *Opt Express*. 2011;19(22):21652–21657.

- [15] Li Z, Ma Y, Huang R, et al. Manipulating the plasmon-induced transparency in terahertz metamaterials. *Opt Express*. 2011;19(9):8912–8919.
- [16] Lezama A, Akulshin AM, Barreiro S. Electromagnetically induced absorption. *Phys Rev A*. 1999;59(6):4732–4725.
- [17] Sun Y, Tan W, Liang L, et al. Metamaterial analog of quantum interference: from electromagnetically induced transparency to absorption. *Epl-Europhys Lett*. 2012;98(6):64007.
- [18] Tassin P, Zhang L, Zhao R, et al. Electromagnetically induced transparency and absorption in metamaterials: the radiating two-oscillator model and its experimental confirmation. *Phys. Rev. Lett*. 2012;109(18):187401.
- [19] Zhang FL, Huang XC, Cai WQ, et al. EIA metamaterials based on hybrid metal/dielectric structures with dark-mode-enhanced absorption. *Opt Express*. 2020;28(12):17481–17489.
- [20] Zhang XQ, Xu NN, Qu KN, et al. Electromagnetically induced absorption in a three-resonator metasurface system. *Sci Rep*. 2015;5(1):10737.
- [21] Lv Y, Zhu DD, Sun YZ, et al. Transition from electromagnetically induced transparency to electromagnetically induced absorption utilizing phase-change material vanadium dioxide based on circularly polarized waves. *Phys E*. 2023;145:115507.
- [22] Zhu DD, Lv Y, Li SY, et al. Broadband plasmon-induced transparency to a electromagnetically induced absorption conversion metastructure based on germanium. *Ann Phys*. 2023;535(1):2200425.
- [23] Zhao Y, Alu A. Manipulating light polarization with ultrathin plasmonic metasurfaces. *Phys Rev B*. 2011;84(20):205428.
- [24] Chang CC, Zhao Z, Li D, et al. Broadband linear-to-circular polarization conversion enabled by birefringent off-resonance reflective metasurfaces. *Phys Rev Lett*. 2019;123(23):237401.
- [25] Ye Y, He S. 90° polarization rotator using a bilayered chiral metamaterial with giant optical activity. *Appl Phys Lett*. 2010;96(20):203501.
- [26] Foteinopoulou S, Kafesaki M, Economou EN, et al. Two-dimensional polaritonic photonic crystals as terahertz uniaxial metamaterials. *Phys Rev B*. 2011;84(3):035128.
- [27] Baena JD, Del Risco JP, Slobozhanyuk AP, et al. Self-complementary metasurfaces for linear-to-circular polarization conversion. *Phys Rev B*. 2015;92(24):245413.
- [28] Dong J, Ding C, Mo J. A low-profile wideband linear-to-circular polarization conversion slot antenna using metasurface. *Materials*. 2020;13(5):1164.
- [29] Mutlu M, Ozbay E. A transparent 90° polarization rotator by combining chirality and electromagnetic wave tunneling. *Appl Phys Lett*. 2012;100(5):051909.
- [30] Sun WJ, He QO, Hao JM, et al. A transparent metamaterial to manipulate electromagnetic wave polarizations. *Opt Lett*. 2011;36(6):927–929.
- [31] Sun YZ, Guo ZH, Gao CJ, et al. Tunable polarization comb based on the electromagnetically induced transparency with hybrid metal-graphene metamaterial. *Phys Scr*. 2021;96(12):125539.
- [32] Zhou KM, Caroopen S, Delorme Y, et al. Dielectric constant and loss tangent of silicon at 700–900 GHz at cryogenic temperatures. *IEEE Micro Wirel Co*. 2019;29(7):501–503.
- [33] Sun YZ, Zhang D, Zhang HF. Tailoring dual-band electromagnetically induced transparency with polarization conversions in a dielectric-metal hybrid metastructure. *Opt Express*. 2022;30(17):30574–30591.
- [34] Zhang H, He XC, Zhang D, et al. Multitasking device with switchable and tailored functions of ultra-broadband absorption and polarization conversion. *Opt Express*. 2022;30(13):23341–23358.
- [35] Sun YZ, Gao CJ, Qu J, et al. Circularly polarized manipulations with VO<sub>2</sub>-doped dielectric electromagnetically induced transparency and absorption. *Ann Phys*. 2022;534(6):2200130.
- [36] Ma CJ, Zhang YB, Zhang Y, et al. All-optical tunable slow-light based on an analogue of electromagnetically induced transparency in a hybrid metamaterial. *Nanoscale Adv*. 2021;3(19):5636–5641.
- [37] Lu H, Liu X, Mao D. Plasmonic analog of electromagnetically induced transparency in multi-nanoresonator-coupled waveguide systems. *Phys Rev A*. 2012;85(5):053803.
- [38] Jiang L, Pan Y, Yi AL, et al. Trading off security and practicability to explore high-speed and long-haul chaotic optical communication. *Opt Express*. 2021;29(8):12750–12762.

- [39] Zeng L, Zhang HF. Absorption improvement of the anapole metastructure for sensing applications. *IEEE Sens J.* [2022](#);22(12):11644.
- [40] Zhu L, Meng FY, Liang D, et al. Polarization manipulation based on electromagnetically induced transparency-like (EIT-like) effect. *Opt Express.* [2013](#);21(26):32099–32110.
- [41] Guo ZH, Sun YZ, Zeng L, et al. Temperature-controlled and photoexcited multitasking Janus metasurface in the terahertz region. *Ann Phys.* [2022](#);534(5):2100499.
- [42] Gao CJ, Zhang D, Zhang HF. Simultaneously achieving circular-to-linear polarization conversion and electromagnetically induced transparency by utilizing a metasurface. *Ann Phys.* [2022](#);534(4):2100578.
- [43] Zhao XG, Schalch J, Zhang JD, et al. Electromechanically tunable metasurface transmission waveplate at terahertz frequencies. *Optica.* [2018](#);5:303–310.
- [44] Khanikaev AB, Mousavi SH, Wu C, et al. Electromagnetically induced polarization conversion. *Opt Commun.* [2012](#);285(16):3423–3427.
- [45] Zhu L, Zhao X, Miao FJ, et al. Dual-band polarization convertor based on electromagnetically induced transparency (EIT) effect in all-dielectric metamaterial. *Opt Express.* [2019](#);27(9):12163–12170.
- [46] Grad NK, Heyes JE, Chowdhury DR, et al. Terahertz metamaterials for linear polarization conversion and anomalous refraction. *Science.* [2013](#);340(6138):1304–1307.
- [47] He JN, Ding P, Wang JQ, et al. Ultra-narrow band perfect absorbers based on plasmonic analog of electromagnetically induced absorption. *Opt Express.* [2015](#);23(5):6083–6091.
- [48] Taubert R, Hentschel M, Giessen H. Plasmonic analog of electromagnetically induced absorption: simulations, experiments, and coupled oscillator analysis. *JOSA B.* [2013](#);30(12):3123–3134.
- [49] Bagci F, Mulazimoglu C, Can S, et al. A glass based dual band frequency selective surface for protecting systems against WLAN signals. *AEU Int J Electron C.* [2017](#);82:426–434.
- [50] Chen X, Li YQ, Fu YQ, et al. Design and analysis of lumped resistor loaded metamaterial absorber with transmission band. *Opt Express.* [2012](#);20(27):28347–28352.
- [51] Zhang YG, Wu JB, Liang LJ. Effect of loss and coupling on the resonance of metamaterial: an equivalent circuit approach. *Sci China Inform Sci.* [2014](#);57(12):1–8.
- [52] Jiang YN, Wang L, Wang J, et al. Ultra-wideband high-efficiency reflective linear-to-circular polarization converter based on metasurface at terahertz frequencies. *Opt Express.* [2017](#);25(22):27616–27623.